



Published in final edited form as:

Nat Neurosci. 2017 July ; 20(7): 905–916. doi:10.1038/nn.4561.

Reduced sensory synaptic excitation impairs motor neuron function via Kv2.1 in spinal muscular atrophy

Emily V. Fletcher^{1,2}, Christian M. Simon^{1,2}, John G. Pagiazitis^{1,2}, Joshua I. Chalif^{1,2}, Aleksandra Vukojicic^{1,2}, Estelle Drobac^{1,2}, Xiaojian Wang^{1,2}, and George Z. Mentis^{1,2,3,*}

¹Center for Motor Neuron Biology and Disease, Columbia University, New York, NY, 10032, USA

²Department of Pathology and Cell Biology, Columbia University, New York, NY, 10032, USA

³Department of Neurology, Columbia University, New York, NY, 10032, USA

Abstract

Behavioral deficits in neurodegenerative diseases are often attributed to the selective dysfunction of vulnerable neurons via cell-autonomous mechanisms. Although vulnerable neurons are embedded in neuronal circuits, the contribution of their synaptic partners to the disease process is largely unknown. Here, we show that in a mouse model of spinal muscular atrophy (SMA), a reduction in proprioceptive synaptic drive leads to motor neuron dysfunction and motor behavior impairments. In SMA mice or after the blockade of proprioceptive synaptic transmission we observed a decrease in the motor neuron firing which could be explained by the reduction in the expression of the potassium channel Kv2.1 at the surface of motor neurons. Increasing neuronal activity pharmacologically by chronic exposure *in vivo* led to a normalization of Kv2.1 expression and an improvement in motor function. Our results demonstrate a key role of excitatory synaptic drive in shaping the function of motor neurons during development and the contribution of its disruption to a neurodegenerative disease.

Movement is an essential behavior that is controlled by motor circuits. The intricate assembly of motor circuits is established by genetic programs¹ and is subsequently refined by synaptic activity². Within spinal motor circuits, motor neurons (MNs) bridge the central and peripheral nervous systems by conveying central commands to the skeletal muscles. MNs receive synapses from sensory neurons³, spinal interneurons⁴ and supraspinal pathways⁵. However, the underlying mechanisms of how neurotransmission shapes MN

Users may view, print, copy, and download text and data-mine the content in such documents, for the purposes of academic research, subject always to the full Conditions of use: http://www.nature.com/authors/editorial_policies/license.html#terms

*Correspondence to: gzmentis@columbia.edu.

Author's contributions

G.Z.M. conceived the project. E.V.F. and G.Z.M. designed the experiments. E.V.F. performed all intracellular experiments and data analysis. E.V.F., J.P., C.M.S., A.V., and E.D. performed immunohistochemical experiments, motor neuron retrograde labeling, synaptic analysis, NMJ analysis and motor neuron counts. E.V.F., C.M.S., E.D. and J.P. performed behavioral analysis. C.M.S. performed Western blot experiments. E.V.F., J.P., J.I.C., E.D. and G.Z.M. performed *in vivo* experiments. X.W. and J.P. performed genotyping and assisted in synaptic analysis. G.Z.M. performed NMJ functional studies. G.Z.M. wrote the manuscript with input from all authors.

Competing Financial Interests Statement

The authors declare no competing financial interests.

output are undefined. Furthermore, genetic perturbations causing neurodegenerative diseases may lead to synaptic and circuit dysfunction and initiate the demise of normal behavior.

In neurodegenerative diseases, behavioral impairment is attributed to the dysfunction of a specific neuronal type, which is distinctly vulnerable to a ubiquitous gene mutation⁶. Dysfunction of select neurons acting as the primary targets of disease-causing mutations may precipitate secondary changes to their synaptic partners and exacerbate the disease⁷. Whether and how neuronal dysfunction in principally affected neurons may cause dysfunction of their synaptic partners and impact pathogenesis has not been established.

Here, we used a mouse model of spinal muscular atrophy (SMA), an inherited neurodegenerative disease, to investigate the impact of non-cell autonomous mechanisms in the pathogenesis of disease. SMA is characterized by MN death, muscle atrophy and motor impairment⁸. Patients have homozygous mutations in the ubiquitous *survival motor neuron 1* (*SMN1*) gene, but retain copies of a nearly identical hypomorphic gene *SMN2*^{9,10}, causing SMN protein deficiency¹⁰. SMN dysfunction in neurons, but not in muscles, underlies motor impairment in mouse¹¹ and fly¹² SMA models. We have shown that synaptic dysfunction occurs simultaneously with MN hyperexcitability, preceding MN death¹³. Whether synaptic dysfunction is responsible for the MN hyperexcitability or synaptic loss occurs in response to MN dysfunction is unresolved. The primary neuronal target(s) affected by SMN-deficiency leading to SMA motor circuit dysfunction remain elusive.

We report that SMA MNs increase their input resistance but exhibit decreased firing as a result of sensory-motor synapse dysfunction. Strikingly, both characteristics of MN dysfunction are rescued by selective SMN restoration in proprioceptive neurons. Further, synaptic dysfunction is characterized by impaired glutamate release, accompanied by a reduction of Kv2.1 channel expression in SMA MNs. The reduction of Kv2.1 is reversed by SMN restoration in proprioceptive neurons and pharmacologically-induced increase in network activity. Our findings elucidate cellular and network mechanisms responsible for SMA pathology and identify sensory excitatory synaptic drive as a major determinant in regulating MN output.

RESULTS

Motor neuron dysfunction onset correlates with proprioceptive synaptic impairment in SMA

SMA MNs exhibit selective vulnerability depending on the muscles they innervate, with proximal muscles more affected than distal muscles in mice¹⁴ and humans¹⁵. We previously reported that SMA MNs in the first lumbar segment (L1) exhibit an increase in input resistance early in the disease¹³. Whether vulnerable SMN-deficient MNs become dysfunctional as a result of synaptic impairment or due to MN-autonomous mechanisms is unknown. To study vulnerable MNs, we focused on those that innervate the iliopsoas (IL) and quadratus lumborum (QL) muscles^{13,14}. These muscles are involved in maintaining posture and locomotion¹⁵ and are involved in the righting reflex which is impaired in SMA mouse models¹³. The IL/QL MNs reside within the L1 to L3 spinal segments¹⁶. Tracing

experiments from muscle together with ventral root L2 fill, indicated that the largest portion of IL/QL MNs lie laterally within the L2 spinal segment (Supplementary Fig. 1).

The excitability of a neuron is defined by its ability to generate action potentials in response to injected currents or synaptic inputs and is regulated by its intrinsic membrane properties. To study the intrinsic passive and active membrane properties and monosynaptic sensory-induced synaptic potentials of L2 MNs, we employed whole-cell current clamp recordings using the intact mouse spinal cord *ex vivo* preparation¹³ at P2 (Supplementary Fig. 2A). Analysis of the intrinsic membrane properties of SMA MNs revealed two populations (Supplementary Fig. 2B). 57% were similar to WT MNs (“SMA-unaffected”), while 43% exhibited signs of dysfunction (“SMA-affected”), evident by significantly increased input resistance and time constant and reduced rheobase (Fig. 1A–E). To investigate whether resistant SMA MNs were also affected, we studied L5 lateral MNs, which innervate the distal hindlimb muscles gastrocnemius and tibialis anterior, at P4. We found no difference in the intrinsic membrane properties of WT and SMA L5 MNs even at this later stage of the disease (Supplementary Fig. 2C–E). Thus, ubiquitous SMN deficiency in MNs does not cause dysfunction in all spinal MNs, further highlighting the selective vulnerability of specific MN pools.

To determine the basis of MN dysfunction in L2 SMA-affected MNs, we first quantified the number of proprioceptive synapses on their somata and proximal dendrites. We employed retrograde tracing to label the somatodendritic tree of MNs¹³ together with immunohistochemistry against the Vesicular Glutamate Transporter 1 (VGluT1) (Fig. 1F), a marker of proprioceptive synapses¹⁷. We found a modest overall reduction in VGluT1 synapses on the SMA MNs, considering that there was no synaptic loss on dendrites (Fig. 1G), where over 90% of the proprioceptive synapses make contact with motor neurons^{13,18}. Furthermore, analysis of the number of VGluT1 synapses on the transverse area of the MN soma revealed that all SMA L2 MNs are equally affected (Supplementary Fig. 2H–I). Thus, the loss of proprioceptive synapses on the soma is unlikely to be the main contributor to increased input resistance in SMA MNs.

Next we analyzed the monosynaptically-induced excitatory postsynaptic potential (EPSP) following proprioceptive fiber stimulation. While SMA-unaffected MNs exhibited comparable EPSP amplitudes to WT MNs, SMA-affected hyperexcitable MNs exhibited reduced EPSPs (Fig. 1H–I). Resistant L5 SMA MNs exhibited similar EPSP amplitudes compared to WTs (Supplementary Fig. 2F–G). These results highlight a strong relationship between synaptic function and intrinsic membrane properties of MNs, suggesting that synaptic dysfunction precedes synaptic loss and induces an increase in MN input resistance early in disease.

Loss of SMN from proprioceptive neurons weakens sensory-motor synapses and causes motor neuron dysfunction

To define the cellular basis of sensory-motor circuit dysfunction in SMA, we restored SMN specifically in proprioceptive neurons, or in MNs, or in both neuronal classes in SMA mice. We used a mouse model of SMA harboring a single targeted mutation and two transgenic alleles, resulting in the following genotype *Smn*^{+/*Res*};*SMN2*^{+/*+*};*SMN* *7*^{+/*+*}¹⁹. The allele

carrying the targeted mutation (*Smn^{Res}*) is engineered to revert to a fully functional *Smn* allele upon Cre-mediated recombination (*Cre^{+/-};Smn^{Res/-};SMN2^{+/+};SMN 7^{+/+}*)¹⁹. *SMN2* is the human gene and *SMN 7* corresponds to the human SMN cDNA lacking exon 7. In the absence of the Cre recombinase (*Cre^{-/-};Smn^{Res/-};SMN2^{+/+};SMN 7^{+/+}*) the phenotype of these mice is similar to that of the SMN 7 SMA mice¹⁹ and this approach has been validated in several studies¹⁹⁻²¹.

Restoration of SMN protein in proprioceptive neurons was achieved by crossing the conditional inversion SMA mice with Parvalbumin::Cre (Pv^{Cre}) mice. Parvalbumin is expressed exclusively in proprioceptive neurons during the first 10 postnatal days²² and is similar in WT and SMA mice (Supplementary Figs. 3A–B). Parvalbumin was expressed in the cerebellum at P5 (Supplementary Figs. 3A–B) and behaviors known to depend on cerebellar activity, including postural control and balance, reveal a marked increase in efficiency at ~P14 in neonatal rats²³ and are unlikely to have a major effect during the first postnatal week. Experimentally, transection at a high medula level revealed that cerebellar activity did not significantly impact the righting reflex of P3 WT mice (Supplementary Figs. 3C–D). Additionally, SMA vulnerable slow twitch muscles like the QL²⁴ did not express parvalbumin (Supplementary Fig. 4). The same results are observed in Pv^{Cre}::Isl-TdTomato mice (Supplementary Fig. 5). Restoration of SMN in MNs was achieved by crossing the conditional inversion SMA mice with those expressing Cre under the ChAT promoter (SMA+ChAT^{Cre}). We investigated Cre efficacy by crossing the Pv^{Cre} and ChAT^{Cre} with Isl-TdTomato mice and found that 95% of ChAT+ MNs expressed TdTomato, and 91% of Parvalbumin+ neurons in the dorsal root ganglion (DRG) expressed TdTomato (Supplementary Fig. 6A–B). Immunohistochemistry against Cre revealed that 89% of ChAT+ MNs expressed Cre in ChAT^{Cre} mice and 87% of Pv+ proprioceptive neurons expressed Cre in Pv^{Cre} mice (Supplementary Fig. 6C–D). To examine the efficacy and specificity of SMN upregulation following Cre recombination in proprioceptive and MNs, we used SMN immunohistochemistry to study the presence of Gems, nuclear structures containing SMN²⁵, in proprioceptive and MNs in the L2 spinal segment at P4 (Supplementary Fig. 6E–H). We found 93% of WT proprioceptive neurons expressed Gems, compared to none in SMA and 60% in SMA+Pv^{Cre} mice (Supplementary Fig. 6G). Similarly, 81% of WT MNs expressed Gems and 50% in SMA+ChAT^{Cre} mice (Supplementary Fig. 6H), confirming selective SMN restoration in the majority of proprioceptive and MNs.

To address the cellular origin of the increased input resistance of SMA MNs, we investigated the effects of selective SMN restoration in either proprioceptive or MNs at P4. At this age, ~85% of SMA MNs exhibited an increase in input resistance and time constant (Fig. 2A–B), revealing a progressive pathology in L2 SMA MN function over the first neonatal week. To rule out a reduction in soma size explaining the increased input resistance, measurements of whole-cell capacitance revealed no differences between WT and SMA MNs (Fig. 2B). Furthermore, comparison of the soma size from WT and SMA motor neurons, filled with Neurobiotin during intracellular recordings, revealed no statistical difference (Supplementary Fig. 7A–D). Strikingly, the increased input resistance of SMN-deficient MNs was corrected to WT levels in SMA+Pv^{Cre} mice, while restoration of SMN in only MNs (SMA+ChAT^{Cre}) had no effect (Fig. 2A–B). Therefore, increased input resistance of SMA MNs is mediated by non-cell autonomous mechanisms.

Next, we measured the EPSP amplitude in L2 MNs following proprioceptive fiber stimulation at P4. We did not observe any significant changes in the MN resting membrane potential for any of the experimental groups at P4 (WT: -55.9 ± 1.8 mV, SMA: -52.9 ± 1.5 mV; SMA+Pv^{Cre}: -53.0 ± 2.1 mV; SMA+ChAT^{Cre}: -52.5 ± 2.3 mV; N.S., One Way ANOVA). Importantly, the reduction of the EPSP amplitude in SMA MNs was restored in SMA+Pv^{Cre} but not in SMA+ChAT^{Cre} MNs (Fig. 2C–D). Furthermore, analysis of the EPSP amplitude and input resistance (Fig. 2E) demonstrates that MNs exhibiting large EPSPs possess low input resistances. This relationship is similar in WT and SMA+Pv^{Cre} MNs (Fig. 2E). To address whether the reduction in EPSP amplitude is due to impaired glutamate release, we performed paired-pulse stimulation of the dorsal root at 1Hz. Proprioceptive-induced EPSPs in WT mice were mildly depressed at P4 as previously reported²⁶. However, EPSPs in SMA mice were significantly more depressed than WTs (Fig. 2F–G). This depression was corrected in SMA+Pv^{Cre} mice, but not in SMA+ChAT^{Cre} mice (Fig. 2F–G). Thus, the reduction of EPSPs in SMA is due to impairment of glutamate release.

To address whether the improved EPSP amplitude in SMA+Pv^{Cre} MNs was due to a rescue of proprioceptive synapses or enhanced presynaptic function of the remaining synapses, we analyzed the number of VGluT1+ synapses on retrogradely filled MNs. There was a significant rescue of VGluT1 synapses both on the somata and dendrites of MNs in SMA+Pv^{Cre} mice at P4 (Fig. 2H–J), whereas SMA+ChAT^{Cre} MNs showed no rescue (Fig. 2H–J). Furthermore, we found that VGluT1 synapses in SMA+Pv^{Cre} remained comparable to WT synaptic numbers at P11, a late stage of disease (Supplementary Fig. 8A–C), demonstrating that proprioceptive synapses continue to develop. Thus, restoration of SMN in proprioceptive neurons rescues synaptic loss. Collectively, our results demonstrate that MN dysfunction is a non-cell autonomous consequence of SMN-dependent deficits in proprioceptive neurons.

Dysfunction and death of motor neurons are two independent events in SMA

MN death is a hallmark of SMA¹⁰. MN hyperexcitability has been implicated in neuronal death following axotomy of facial MNs²⁷ and in ALS²⁸. We therefore asked, whether selective SMN upregulation in proprioceptive neurons affected the survival of SMA MNs. We demarcated the L2 rostrocaudal extent as we previously described¹³ and counted all L2 MNs identified by ChAT staining at P2, P4 and P11. There was no significant MN loss at P2, but 34% of MNs were lost at P4 and 42% at P11 (Fig. 3A–B). SMN restoration in proprioceptive neurons only (SMA+Pv^{Cre}) did not result in any significant rescue, whereas selective restoration in MNs (SMA+ChAT^{Cre}) resulted in rescue of MNs both at P4 and at P11, which was not ameliorated any further by SMA+(Pv+ChAT)^{Cre} mice (Fig. 3A–B). These results demonstrate that SMN-deficiency in sensory neurons does not induce the death of MNs. Thus, dysfunction and death of MNs are distinct and independent events, likely governed by different mechanisms.

Dysfunction of proprioceptive synapses causes reduction in motor neuron firing in SMA

The effects of increased input resistance on neuronal firing in neurodegenerative diseases are poorly understood. To address this, we analyzed the firing frequency in L2 MNs following current injection. WT and SMA P2 MNs, fired repetitively at variable strengths of current

injection (Supplementary Fig. 9A–C). Thus, we compared the MN firing frequency among the groups, induced by steps of current above the minimum current required for repetitive firing. The firing frequency of SMA-unaffected MNs was indistinguishable from control MNs (Fig. 4A–B). However, SMA-affected MNs, despite exhibiting increased input resistance (Fig. 1A–E), paradoxically displayed reduced firing rates compared to controls at P2 (Fig. 4A–B). Importantly, SMA resistant L5 MNs, which did not exhibit increased input resistance, did not display any significant changes in firing frequency (Supplementary Fig. 9D–E).

At P4, when nearly all SMA L2 MNs exhibit increased input resistance, all SMA MNs fired at significantly lower frequencies (Fig. 4C–D). Remarkably, SMA+Pv^{Cre} MNs exhibited a significant correction in firing frequency (Fig. 4C, E), whereas SMA+ChAT^{Cre} MNs fired at similar frequencies to SMA MNs (Fig. 4C, F). Although SMA MNs exhibited a reduction in the voltage threshold (V_{thr}) compared to WT (WT: -26.6 ± 1.7 mV; SMA: -39.7 ± 2.4 mV; $p=0.0011$, Mann-Whitney) in agreement with our previous report¹³, SMA+Pv^{Cre} and SMA+ChAT^{Cre} MNs had similar V_{thr} values to SMA MNs. Thus, SMA MNs fire at significantly reduced frequencies and this reduction is possibly triggered by the dysfunction of sensory-motor synapses.

SMN upregulation in proprioceptive neurons in SMA mice improves NMJ function and motor behavior

We next investigated the effects of selective restoration of SMN in proprioceptive neurons at the neuromuscular junction (NMJ) by examining the functional and morphological properties of NMJs in the vulnerable QL muscles of SMA mice, at P4. We found that the QL exhibited 37% denervation in SMA mice and 38% in SMA+Pv^{Cre} mice (Fig. 5A–B). In contrast, we observed a complete rescue of NMJ denervation when SMN was restored in MNs only (SMA+ChAT^{Cre}) or in both neuronal classes [SMA+(Pv+ChAT)^{Cre}] (Fig. 5A–B). Next, we developed an assay that measures NMJ function by stimulating MN axons in the L2 ventral root and recording the resultant compound muscle action potential (CMAP) in the QL muscle (Supplementary Fig. 10A). This assay is uncontaminated by electrical activity from motor axons because exposure to pancuronium results in complete abolition of the CMAP (Supplementary Fig. 10C).

We found that the CMAP amplitude was significantly reduced in SMA mice (Fig. 5C–D). Strikingly, selective upregulation of SMN in SMA+Pv^{Cre} mice resulted in a significant improvement ($\times 2.3$ fold increase) in CMAP amplitude, while SMA+ChAT^{Cre} mice exhibited a more robust ($\times 3.8$ fold increase) improvement (Fig. 5C–D). Restoration of SMN in both neuronal types resulted in recovery to WT levels (Fig. 5C–D). To assess CMAP reliability, a train of stimuli at 20 Hz (Supplementary Fig. 10B) revealed that WT, SMA+ChAT^{Cre} and SMA+(Pv+ChAT)^{Cre} were able to induce reliable CMAP responses (Fig. 5E–F). In contrast, SMA and SMA+Pv^{Cre} exhibited $\sim 35\%$ decline by the end of the stimulus train. Thus, SMN restoration in proprioceptive neurons moderately improves NMJ function, but not denervation.

To assess the behavioral benefits of selective SMN restoration in proprioceptive neurons, MNs, or both neuronal populations, we analyzed the righting time of SMA mice. We found

that SMA+Pv^{Cre} mice exhibited improved righting time as early as P3 (Fig. 5G) and modestly increased lifespan (Supplementary Fig. 10D). Furthermore, while selective restoration of SMN in MNs improved the righting time (Fig. 5H) and increased lifespan (Supplementary Fig. 10E) as previously reported²⁰, combinatorial SMN upregulation in both proprioceptive and MNs [SMA+(Pv+ChAT)^{Cre}] revealed a synergistic improvement of motor behavior compared to SMA+ChAT^{Cre} mice (Fig. 5H). These results demonstrate that SMN deficiency in proprioceptive neurons significantly contributes to the motor deficits in SMA.

Block of neurotransmitter release from proprioceptive synapses causes motor neuron dysfunction during early development

To tease out the synaptic mechanisms responsible for MN dysfunction, we investigated whether impaired glutamate release from proprioceptive synapses is responsible for the increased input resistance and reduced firing frequency of MNs. We blocked neurotransmission at proprioceptive synapses through expression of the tetanus toxin light chain subunit (TeNT), which inhibits neurotransmitter release²⁹. A Pv^{Cre} driver mouse line was crossed to a ROSA26^{Isl-TeNT} mouse strain³⁰ to generate Pv^{TeNT} mice. Pv^{TeNT} mice have a short life-span, surviving on average until P18 and exhibit severe defects in motor coordination, including a nearly complete inability to right during the first four postnatal days (Fig. 6A). As we reported recently²², these mice display nearly complete (~97%) block of neurotransmission from proprioceptive synapses on MNs. Pv^{TeNT} mice showed no loss of VGluT1 synapses from the somata and proximal dendrites of L2 MNs (Fig. 6B–D). However, Pv^{TeNT} L2 MNs exhibited a significantly increased input resistance and time constant and reduced rheobase (Fig. 6E–I). These changes were not due to a reduction in MN size since the capacitance did not change (Fig. 6H). L5 Pv^{TeNT} MNs also increased their input resistance (Supplementary Fig. 11F–H), suggesting that glutamatergic block from proprioceptive synapses causes input resistance changes in all MNs and is not specific to certain MN pools. Furthermore, frequency-current plots from L2 Pv^{TeNT} MNs at P4 revealed a significant reduction in firing frequency (Fig. 6J–K), indicating that neurotransmission block at sensory-motor synapses impacts MN firing frequency. There was no significant loss of L2 MNs (Supplementary Fig. 11A), NMJ denervation in the QL muscle (Supplementary Fig. 11B–C) or significant changes in CMAP amplitude (Supplementary Fig. 11D and E).

To test the possibility that signaling from factors such as BDNF - known to be released by proprioceptive neurons^{31,32} - may also be responsible for MN dysfunction, we overexpressed BDNF in SMA mice by transducing proprioceptive neurons with AAV9-GFP-mBDNF, injected intra-cerebro-ventricularly at birth and examined the function of SMA MNs at P5 (see Online Methods and Supplementary Fig. 12). Approximately 85% of proprioceptive neurons and 50% of MNs were transduced (Supplementary Fig. 12A–D). BDNF release from SMA proprioceptive synapses was confirmed by an increase of GAD65 - but not GAD67 - in GABApre synapses (Supplementary Fig. 12E–H), as we reported for VGluT1^{-/-} mice³². To avoid the effects of direct BDNF overexpression in SMA MNs, we only analyzed non-transduced SMA MNs (Supplementary Fig. 12I). Thus, any possible changes would be due to overexpression of BDNF in proprioceptive neurons. We found that non-transduced SMA MNs exhibited similar increases in input resistance and reduced firing

frequency compared to SMA control MNs (Supplementary Fig. 12I–L). Taken together, these results suggest that changes in SMA MN function are unlikely to be mediated by BDNF release from proprioceptive neurons.

Collectively, these results demonstrate that block of glutamate release at sensory-motor synapses results in increased MN input resistance and a concomitant reduction in firing frequency, but not MN death, phenocopying aspects of SMA. Thus, presynaptic function impairment is likely responsible for MN dysfunction in SMA.

Sensory-motor synaptic dysfunction in SMA leads to a widening of the motor neuron spike waveform

We sought to decipher the molecular mechanisms of MN dysfunction, causally linking the reduction in firing frequency with decreased sensory-motor excitatory synaptic drive, by comparing the orthodromically-induced action potential profiles of SMA and WT MNs during steady-state repetitive firing induced by current injection. We found that the afterhyperpolarization (AHP) is unlikely to contribute to the reduction in spiking frequency in SMA MNs, because there was no significant difference in either AHP amplitude or duration (Supplementary Fig. 13A–B). Examination of the action potential duration revealed significantly prolonged action potentials in SMA MNs compared to WT controls as illustrated by the increase of the action potential half-width (Fig. 7A–B). Importantly, SMA +Pv^{Cre} MNs exhibited action potentials similar to those observed in WTs, while action potentials in SMA+ChAT^{Cre} MNs were similar to SMA MNs (Fig. 7A–B). Furthermore, Pv^{TeNT} MNs exhibited prolonged action potentials akin to SMA MNs (Fig. 7C–D). Although the rate of depolarization in action potentials was similar amongst the four experimental groups (WT: 36.7±3.1; SMA: 34.8±4.0; SMA+Pv^{Cre}: 29.4±1.2; SMA +ChAT^{Cre}: 33.8±6.6 mV/ms, N.S., ANOVA), the rate of repolarization was significantly slower in SMA and SMA+ChAT^{Cre} MNs and it was corrected in SMA+Pv^{Cre} MNs (WT: 18.9±2.0; SMA: 10.5±1.1; SMA+Pv^{Cre}: 14.3±0.9; SMA+ChAT^{Cre}: 9.4±1.7 mV/ms; p=0.004 in WT vs SMA and p=0.002 in WT vs SMA+ChAT^{Cre}, ANOVA). Thus, widening of the spike waveform is likely responsible for the reduced output seen in SMA MNs.

Loss of SMN from proprioceptors reduces the surface expression of Kv2.1 in motor neurons

The slower repolarization of the action potential raised the possibility that changes in potassium channels may be responsible for spiking frequency reduction. The “delayed rectifier” Kv2.1 channel plays an important role in action potential repolarization in MNs³³. We therefore investigated the contribution of Kv2.1 channels to SMA MN dysfunction. We compared the half-width of action potentials and MN firing frequency following acute exposure to the specific blocker of Kv2 channels, Guangxitoxin-1E (GxTx-1E)^{34,35}. GxTx-1E specifically blocks Kv2.1 and Kv2.2 at 100 nM and Kv4.3 at higher concentrations³⁴. Exposure to 100 nM GxTx-1E did not alter the input resistance of WT and SMA MNs (Supplementary Fig. 13C–E). The action potential half-width was significantly increased in WT but only marginally increased in SMA MNs (Fig. 7E–G). Importantly, the firing frequency following current injection was significantly reduced in WT MNs, and less affected in SMA MNs (Fig. 7H–J). An insight to explain how the reduction in Kv2 current

reduces the firing ability is revealed by measurements of the trough voltage, defined as the most negative potential between two spikes during repetitive firing (Supplementary Fig. 13F). We found a significant increase in the trough voltage, with a shift to more depolarized potentials, in SMA MNs compared to WT mice when the firing frequency doubles (Supplementary Fig. 13G). This depolarization may result in a reduced recovery of voltage-gated sodium channels from inactivation, ultimately limiting sodium channel availability for the initiation of subsequent spikes and thereby reducing firing frequency. Collectively, these results indicate that the reduction in spiking frequency in SMA MNs is likely due to a reduction in Kv2 potassium channels.

To focus on channel expression in MNs, we performed immunohistochemistry with antibodies against Kv2.1, Kv2.2 and Kv4.3. Kv2.1 in MNs was associated with proprioceptive synapses (Supplementary Fig. 14A). Analysis of Kv2.1 surface coverage on L2 MN somata (Supplementary Fig. 14B–C) revealed a significant reduction of Kv2.1 in SMA (Fig. 8A–B). Moreover, western blot analysis revealed no significant difference in the overall expression of Kv2.1 in L1–L3 ventral horns from WT and SMA mice (Fig. 7I), indicative of a specific reduction in MNs. The effects are specific for Kv2.1 since Kv2.2 coverage was similar in WT and SMA MNs (Supplementary Fig. 14F) and Kv4.3 is not expressed in MNs at this age (Supplementary Fig. 14G). L5 SMA-resistant MNs, which do not exhibit any reduction in firing frequency, did not display changes in Kv2.1 coverage (Supplementary Fig. 14D–E). In addition, Pv^{TeNT} and SMA+ChAT^{Cre} L2 MNs exhibited a similar reduction in Kv2.1 somatic coverage to SMA MNs (Fig. 8A–B). Similarly, L5 MNs in Pv^{TeNT} mice exhibited a significant reduction in Kv2.1 expression (Supplementary Fig. 14D–E). In striking contrast, SMA+Pv^{Cre} and SMA+(Pv+ChAT)^{Cre} MNs displayed a robust restoration of Kv2.1 coverage to normal levels (Fig. 8A–B). These results demonstrate that reduction of Kv2.1 expression in SMA MNs is a non-cell autonomous consequence of proprioceptive neuron dysfunction.

Chronic postnatal kainate treatment restores normal Kv2.1 surface expression and improves motor function in SMA mice

To test the possibility that Kv2.1 coverage is regulated by excitatory synaptic transmission, we treated SMA mice daily *in vivo* (starting at P0) with kainate, a glutamate receptor agonist. Although kainate has been widely used to induce seizures³⁶, sub-convulsive daily doses of 1.5mg/kg were tolerated for the first postnatal week. Kainate treatment has been shown to increase neuronal activity³⁶. Remarkably, P4 SMA MNs treated with kainate displayed a significant increase in Kv2.1 coverage (Fig. 8A–B), whereas kainate-treated WT MNs did not show any difference in Kv2.1 surface coverage compared to untreated controls (Fig. 8A–B). Additionally, the righting times of SMA mice treated with kainate were significantly improved (Fig. 8C). Thus, an increase in global neuronal activity restores Kv2.1 channel expression and improves motor function in SMA mice.

DISCUSSION

Our study reveals non-cell autonomous mechanisms that shape MN output during development and identifies a functional cascade of synaptic deficits that likely underlie

muscle paralysis in SMA. We show that SMN-deficiency causes sensory-derived dysfunction via the reduction of presynaptic glutamate transmission onto MNs resulting in two opposing effects on their excitability. SMA MNs increase their input resistance but paradoxically reduce their firing ability. This reduction in MN spiking ability is a non-cell autonomous consequence of the decrease in excitatory synaptic drive from proprioceptive neurons, most likely due to the reduction of Kv2.1 channel expression in MNs. Selective restoration of SMN in proprioceptive neurons restores the changes in the membrane properties and spiking frequency of SMA MNs. Accordingly, selective blockade of sensory-motor neurotransmission in the presence of normal SMN levels phenocopied the effects of synaptic dysfunction in SMA. Kainate treatment *in vivo* restored normal Kv2.1 expression and improved motor function, presumably by increasing the excitatory drive onto MNs, and may represent a viable therapeutic approach complementary to SMN upregulation (Supplementary Fig. 15).

Non-cell autonomous mechanisms of SMA motor neuron dysfunction

Neuronal dysfunction is often determined by changes in physiological properties of disease-vulnerable neurons^{13,37}. The intrinsic membrane properties determine neuronal excitability and govern how converging premotor synaptic drive is translated into the generation of action potentials³⁸.

We demonstrated that MN increased input resistance is a non-cell autonomous response induced by SMN-deficiency, ensuing after birth and progressively accumulating in vulnerable SMA MNs, which paradoxically impacts negatively their functional output. First, vulnerable but not resistant SMA MNs exhibit signs of increased input resistance. Second, specific restoration of SMN in MNs does not correct their neuronal membrane properties, whereas restoration of SMN in proprioceptive neurons restores the MN input resistance to normal levels. Lastly, neurotransmission block at proprioceptive synapses (Pv^{TeNT}) phenocopies the changes in the MN membrane properties observed in SMA. Increased input resistance in vulnerable SMA MNs correlates with lower proprioceptive-induced EPSP amplitude, which are both normalized following restoration of SMN in proprioceptive neurons. Thus, SMN deficiency in proprioceptive neurons decreases synaptic release and ultimately precipitates secondary changes in MNs.

Synaptic dysfunction may be caused by compromised presynaptic neurotransmitter release, a loss of synaptic boutons, or both. Early in SMA, the asymmetric reduction in EPSP amplitude (87%) compared to synaptic loss (49%) and the reduction in the paired-pulse stimulation paradigm suggest that the impairment of glutamate release from sensory-motor synapses is the initiating event in SMA. Dysfunction at later stages is further exacerbated by the progressive loss of synapses from dendrites, which comprise ~90% of the total number of synapses¹⁸, and are largely responsible for MN activation³⁹.

Increase in input resistance does not cause cell death

Common events in neurodegenerative diseases are death and dysfunction of vulnerable neurons. Deciphering the mechanisms responsible for these events is key in determining their contribution to the disease process. Increases in the input resistance of MNs are thought

to be linked to neuronal death because axotomy of developing MN axons causes significant cell death²⁷, with subpopulations of MNs exhibiting abnormal increases in input resistance considered to represent a “pre-lethal” stage²⁷. Changes in MN excitability are also associated with neuronal death in ALS^{28,40}. However, a cause-effect relationship between increases in input resistance and death of MNs has not been established. Here, we provide direct evidence that an increase in input resistance and death of MNs are independent, causally-unrelated events induced by SMN deficiency in motor circuits. First, restoration of SMN in proprioceptive neurons restores the functional changes in MNs without rescuing the number of SMA MNs. Second, restoration of SMN in MNs rescues cell-death, consistent with previous studies^{20,41}, but does not correct the changes in input resistance. Finally, neurotransmission block by Pv^{TeNT} increases the MN input resistance, but does not cause MN death. Thus, our work reveals that an abnormal increase in input resistance is not a trigger of MN death.

Impairment of glutamate transmission causes decline in motor neuron output through reduction of Kv2.1 channels

What is the functional relationship between the intrinsic membrane properties and MN output? Changes in firing frequency can be governed by the after-hyperpolarisation⁴² (AHP) and persistent inward currents (PICs)³⁸. However, the reduction of spike firing in SMA is not due to changes in AHP because SMA MNs showed no abnormalities. Similarly, PICs are unlikely to contribute significantly since PICs are cell-autonomously increased in SMA MNs⁴¹. An increase in PICs would be expected to increase the MN firing frequency, but our results in SMA+ChAT^{Cre} mice demonstrated that SMN restoration in MNs did not increase their firing frequency compared to controls. However, GxTx-1E caused a ~10% global reduction in the peak of the action potential and presumably sodium currents, suggesting that PICs may modestly contribute to MN firing.

Spikes evoked at steady-state firing in SMA MNs were broader and were mostly modulated by the potassium channel Kv2.1. SMA MNs decrease their firing frequency because of a reduction in Kv2.1-mediated repolarizing currents, first leading to longer action potentials and subsequently to sustained depolarized voltages between spikes. Extended depolarization would maintain voltage-gated sodium channels in their inactivated state and decrease their availability for action potential generation. Kv2.1 channels are expressed in neurons⁴³, including adult MNs^{44,45}, and are associated with excitatory synapses including proprioceptive inputs⁴⁴, similar to our observations in neonatal MNs. The reduction of Kv2.1 expression in SMA MNs is due to a reduction in glutamate release from proprioceptive synapses rather than their loss, since Kv2.1 was reduced in Pv^{TeNT} animals without synaptic loss. The precise mechanisms for the reduction of Kv2.1 channels are unknown but may include impairments in gene transcription, translation or protein trafficking. Our results identify glutamate release from proprioceptive synapses as a key trigger, and the reduction of Kv2.1 surface expression as the most plausible effector of changes in firing ability of SMA MNs.

Is the increased input resistance and reduction in firing of SMA MNs an adaptive or maladaptive homeostatic response to synaptic dysfunction? Kv2.1 has been described as a

target for mechanisms of homeostatic plasticity⁴⁶. Peripheral axotomy in adult MNs results in Kv2.1 reduction⁴⁵. Since Kv2.1 channels gradually recover after axotomy, it is thought that changes in Kv2.1 expression are a homeostatic response to altered activity⁴⁵. Here, we show that vulnerable SMA MNs, which develop under chronically-reduced glutamate release, exhibit a reduction in firing suggesting that SMA MN dysfunction is a manifestation of an experience-dependent maladaptive response.

Clinical significance for motor neuron disease

Decoding the mechanisms regulating the recruitment of MNs is critical for understanding disease mechanisms. The muscle force produced by a single motor unit is partly determined by muscle fiber number and the frequency at which these fibers are activated by the MN. In humans, the rate at which action potentials activate muscle fibers - known as rate coding - varies considerably, with low frequencies resulting in single twitches and higher frequencies producing fused tetanic contraction^{47,48}. Mice also generate muscle force partly through the rate modulation of motor units⁴⁹. Hence, the firing rate of each motor unit increases with increasing muscular effort until the maximum rate is reached⁵⁰. Since smaller muscles, recruit their motor units within 0–50% maximum voluntary contraction (MVC) they rely exclusively on firing rate increase to augment their force output between 50–100% MVC⁴⁷. Larger muscles recruit human motor units at least to 90% MVC⁴⁷. Thus, smaller muscles rely primarily on firing rate and larger muscles on recruitment order to modulate their force. Here, we show that vulnerable SMA mouse MNs and MNs in Pv^{TeNT} cannot fire at high frequencies, suggesting that the reduced spiking ability greatly contributes to impairment of normal muscle contractions.

In summary, our study demonstrates that a reduction of glutamatergically-mediated neurotransmission from proprioceptive synapses in SMA is a major determinant in shaping MN output. Furthermore, our observations suggest that in SMA patients, although motor units may be recruited more easily resulting in weak twitches of affected muscles, their activation would not reach fused tetanic contractions likely leading to total muscle paralysis as the disease progresses. Therapeutically, our experiments with *in vivo* kainate treatment suggest that an increase in gross synaptic activity could alleviate the severe neurological deficits observed in SMA.

ONLINE METHODS

Animals

All surgical procedures were performed on postnatal mice in accordance with the National Institutes of Health Guidelines on the Care and Use of Animals and approved by the Columbia animal care and use committee (IACUC). Animals of both sexes were used in this study.

The original breeding pairs for the SMA mice used in our study (*Smn*^{+/-}/*SMN2*^{+/+}/*SMN*^{7^{+/+}}) were purchased from Jackson Mice (Jax stock #005025; FVB background) as well as PV^{Cre} (Jax stock #008069) and ChAT^{Cre} (Jax stock #006410). PV^{Cre} and ChAT^{Cre} mice (C57Bl6 background) were bred to generate PV^{Cre}^{+/-};*Smn*^{+/-};*SMN2*^{+/+};*SMN*^{7^{+/+}},

ChAT^{Cre+/-};Smn^{+/-};SMN2^{+/+};SMN 7^{+/+} and *PV^{Cre+/-};ChAT^{Cre+/-};Smn^{+/-};SMN2^{+/+};SMN 7^{+/+}* expressing mice. These strains were bred with SMA mice expressing a *Smn* Cre-inducible allele¹⁹ (*Smn^{Res}*; JAX stock #007951). Cre- SMA mice were null for the *Smn* allele, Cre absent and carrying the *Smn^{Res}* allele (*Smn^{Res/-};SMN2^{+/+};SMN 7^{+/+}*). Cre+ SMA animals were carrying one allele of the *Smn^{Res}*, absent of endogenous mouse *Smn* and heterozygous for either/both *PV^{Cre}* and *ChAT^{Cre}* (*PV^{Cre+/-};Smn^{Res/-};SMN2^{+/+};SMN 7^{+/+}*, *ChAT^{Cre+/-};Smn^{Res/-};SMN2^{+/+};SMN 7^{+/+}*, and *PV^{Cre+/-};ChAT^{Cre+/-};Smn^{Res/-};SMN2^{+/+};SMN 7^{+/+}*). WT mice were homozygous for *Smn* in the absence of Cre (*Smn^{+/+};SMN2^{+/+};SMN 7^{+/+}*). *PV^{Cre}*,⁵¹ and *R26^{floxstop}-TeNT*,³⁰ have been described. *R26^{floxstop}-TeNT* mice were provided by M. Goulding (The Salk Institute) and bred with *PV^{Cre}* mice to obtain *PV^{TeNT}* mice, as published recently²².

Genotyping

Tail DNA PCR genotyping protocols for SMA- 7 mice were followed as described on the Jackson website (www.jax.org). Genotyping for the *R26^{floxstop}-TeNT* allele is described in Zhang et al.³⁰. Customized primers used to genotype the *Smn*, *Smn^{-/-}*, *ChAT^{Cre}*, *PV^{Cre}*, *Smn^{Res}* alleles are listed in Supplementary Table 1. A universal PCR reaction was used as follows: 12.5 µl of GoTaq Hot Start Green Master Mix (Promega), 0.5 µl of each primer (25 µM; Sigma), and 4 µl of 1:20 diluted lysed tail DNA in a final volume of 25 µl using ddH₂O. For the *Smn* and *Smn^{Res}* alleles products were amplified using the following thermal cycling method: 95°C for 2 mins, followed by 35 cycles of 95°C for 1 min, 55°C for 1 min, 72°C for 1 min and 72°C for 5 mins. For the *ChAT^{Cre}* allele: 95°C 3 mins, 97°C 30 s; 2 step cycles 5 times, 95°C 15 s, 69°C 1 min; 3 step cycles 30 times, 95°C 15 s, 60°C 15 s, 68°C 1 min and 68°C for 5 mins. For the *PV^{Cre}* allele: 94°C 3 mins, followed by 35 cycles of, 94°C 30 s, 58°C 30 s, 72°C 1 min and 72°C for 5 min.

Behavioral analysis

Mice from all experimental groups were monitored daily, weighed, and three righting reflex tests were timed and averaged as described previously¹³. Mice with 25% weight loss and an inability to right were euthanized with carbon dioxide to comply with IACUC guidelines. Righting time was defined as the time for the pup to turn over after being placed completely on its back. The cut-off test time for the righting reflex was 60 secs to comply with IACUC guidelines. For systemic administration of kainate (Tocris) P0 – P4 WT and SMA mice were injected daily subcutaneously with a sub-convulsive dose of 1.5 mg/kg dissolved in saline and monitored for body weight and righting times until P4.

Transection experiments

Experiments were conducted on wild type mice at P3. Righting times were first evaluated and averaged following three attempts. Subsequently, pups were anesthetized with isoflurane (5% induction and 2.5% maintenance). After a midline incision in the scalp, a transverse slit was opened through the skull with a pair of forceps, to visualize the cerebellum. Transections were made with a thin, blunt spatula inserted through the slit. The spatula was inserted caudal to the cerebellum and into the brainstem through the slit. The skin was sutured and the pups were returned to their cage following recovery from anesthesia. The

pup's righting ability was evaluated three hours post-transection in the same manner as prior to transection. At the end of the each experiment, animals were perfused with 4% paraformaldehyde (PFA) through transcardial perfusion and the brain was removed. Following an overnight fixation, the brain was embedded in 5% agar and sectioned into 100 μ m sagittal sections using a Vibratome to verify the level and completeness of the transection. Only animals with complete transection at a high medulla level are reported. The sections were not stained and imaged with a stereo-microscope equipped with a Zeiss camera.

Physiology using the intact neonatal spinal cord preparation

Experimental protocols used in this study have been described before¹³. Animals were decapitated and the spinal cords dissected and removed under cold (~12°C) artificial cerebrospinal fluid (aCSF) containing in mM: 128.35 NaCl, 4 KCl, 0.58 NaH₂PO₄·H₂O, 21 NaHCO₃, 30 D-Glucose, 1.5 CaCl₂·H₂O, and 1 MgSO₄·7H₂O. The spinal cord was then transferred to a customized recording chamber placed under the objective of an epifluorescent (Leica DM6000FS) or confocal microscope (Leica SP5). The preparation was perfused continuously with oxygenated (95% O₂/5% CO₂) aCSF (~10 ml/min). Ventral roots and dorsal roots were placed into suction electrodes for stimulation or recording.

Whole-cell recordings were performed at room temperature (~21°C) and obtained with patch electrodes advanced through the lateral aspect of the spinal cord (see Supplementary Fig. 2A). Patch electrodes were pulled from thin-walled borosilicate glass capillary with filament (Sutter Instruments) using a P-1000 puller (Sutter Instruments) to resistances between 5–8 M Ω . The electrodes were filled with intracellular solution containing (in mM): 10 NaCl, 130 K-Gluconate, 10 HEPES, 11 EGTA, 1 MgCl₂, 0.1 CaCl₂ and 1 Na₂ATP, 0.1 Cascade Blue hydrazide (Life Technologies), and in some experiments with 0.5 mg/ml Neurobiotin (Vector Labs). pH was adjusted to 7.2–7.3 with KOH (the final osmolarity of the intracellular solution was 295–305 mOsm). Motor neurons were targeted blindly or in some experiments, from the fluorescence signal following *in vivo* injections of CTb-conjugated to a fluorochrome in the IL/QL muscles at birth, after removal of the dura and pia mater from the lateral aspect of the cord over the L2 spinal segments. The identity of recorded neurons as motor neurons was confirmed by evoking an antidromic action potential by stimulation of the cut ventral root (Supplementary Fig. 2A). Motor neurons were accepted for further analysis only if the following three criteria were met: (i) stable resting membrane potential of –50 mV or more negative (ii) an overshooting antidromically-evoked action potential and (iii) at least 30 mins of recording. The number of animals used for electrophysiology experiments were at P2: 12 WT and 13 SMA animals. At P4: 16 WT, 10 SMA, 8 SMA+Pv^{Cre}, 8 SMA+ChAT^{Cre} and 5 PV^{TeNT} animals.

For the measurements of passive membrane properties, motor neurons were injected with sequential steps of negative and positive currents for 100 ms in 10 pA steps at –60 mV membrane potential. The input resistance (M Ω) was calculated from the slope of the current/voltage plot within the linear range. Membrane time constants (ms) were calculated as 63% of the maximal negative amplitude during the application of the current pulse⁵². The membrane capacitance (M Ω /ms) of each cell was calculated by dividing the input resistance

by the time constant. Measurements were taken from an average of 3 sweeps. We have also determined for a small number of motor neurons that the input resistance does not change across the different SMA mouse lines (SMA vs SMA+ChAT^{Cre-} or SMA+Pv^{Cre-}).

Synaptic potentials were recorded from individual motor neurons (DC - 3 kHz, Multiclamp 700B, Molecular Devices) in response to a brief (0.2 ms) orthodromic stimulation (A365, current stimulus isolator, WPI, Sarasota, FL) of a dorsal root (L2 or L5). The stimulus threshold was defined as the current at which the minimal evoked response was recorded in 3 out of 5 trials. The nerve was stimulated at different multiples of threshold. Recordings were fed to an A/D interface (Digidata 1440A, Molecular Devices) and acquired with Clampex (v10.2, Molecular Devices) at a sampling rate of 10 kHz. Data were analyzed off-line using Clampfit (v10.2, Molecular Devices). The monosynaptic component of the EPSP amplitude was measured from the onset of response to 3 ms⁵³. Measurements were taken from averaged traces of 5 trials elicited at 0.1 Hz. Bridge balance was applied to all recordings. The liquid junction potential was calculated as -5 mV but was not corrected. Measurements were made on averaged traces (3 – 5 trials).

Paired-pulse stimulation experiments were performed and analyzed for all experimental groups at P4. The dorsal root was stimulated at 1 Hz for two stimuli and the resulting motor neuron EPSPs were recorded and analyzed off-line. The amplitude of the 2nd EPSP was expressed as a percentage of the 1st EPSP amplitude. Recording contaminated by spontaneous events or motor neuron depolarizations were discarded.

γ (gamma) motor neurons were not included in our analysis. γ motor neurons were identified by the presence of an antidromic action potential, but lack of direct monosynaptic activation from proprioceptive sensory fibers.

Motor neurons from all experimental groups exhibited a wide range of current required to elicit repetitive firing. To compare statistically the firing frequency in all experimental groups we used steps of current (10 pA) above the minimum current required to elicit repetitive firing for 1 sec. The firing frequency (Hz) was calculated using the event detection function in Clampfit. The last 3 – 5 action potentials during repetitive firing (at the end of the spike train), elicited at 90 pA current injection above the current required to elicit repetitive firing, were isolated and averaged using the “event viewer” function in pClamp. Action potential half-width duration (ms) was measured at the half-maximal spike amplitude. The trough voltage of consecutive action potentials was measured at the most negative voltage in between two spikes³⁵ 1 mM stock solutions of Guangxitoxin-1E (GxTx-1E; Alomone) were prepared in ddH₂O and stored at -20°C. Before electrophysiological recording, 100 nM GxTx-1E was prepared in extracellular solution and administered via the gravity perfusion system for 10 mins before recording. We also performed experiments using 200 nM GxTx-1E, but at this concentration, we found that GxTx-1E had indirect effects on the input resistance, since subsequent exposure to TTX (1 μ M) reversed the increase in the input resistance (data not shown). We did not include in this study any experiments performed with 200 nM GxTx-1E.

The amplitude of the antidromically action potential following ventral root stimulation revealed significant increase in L2 SMA motor neurons compared to their WT counterparts at P4 (mean \pm SEM, WT: 75.4 ± 3.0 mV; SMA: 86.4 ± 3.9 mV ; $P=0.02$, Mann-Whitney), consistent with our previous report in L1 SMA motor neurons (Mentis et al., 2011). In contrast, there was no significant difference in the amplitude of the antidromic AP between WT and SMA L5 motor neurons (mean \pm SEM, WT: 76.9 ± 3.8 mV; SMA: 74.1 ± 3.2 mV; $P=0.85$, unpaired t-test).

After the recording session, in some experiments, the spinal cord was fixed in 4% PFA overnight and subsequently transferred to PBS and processed for immunohistochemistry. In several experiments, intracellularly filled motor neurons from P4 WT and SMA were recovered and revealed with the Avidin-Biotin complex as previously described⁹⁰ to measure the somatic area.

At P2, we observed two populations of motor neurons with respect to changes in input resistance and time constant. We divided these two groups by applying the following criteria and termed them as “affected” and “unaffected” SMA motor neurons. “Unaffected” SMA motor neurons were defined as those SMA motor neurons that exhibited similar correlation between input resistance and time constant to those observed in WT motor neurons. Conversely, “affected” SMA motor neurons, were those motor neurons exhibiting higher values of input resistance and time constant.

Relationship between EPSP amplitude and input resistance

This relationship has been investigated in our previous study¹³. Computer modeling studies have been used to examine the effect of input resistance on the amplitude of monosynaptic EPSPs recorded in adult cat motor neurons in response to stimulation of muscle spindle afferents⁵⁴. The EPSP amplitude is almost linearly proportional to the motor neuron input resistance so that a 3 fold increase in input resistance leads to a 2.8 fold increase in the EPSP amplitude. The input resistance of SMA motor neurons examined in this study is ~ 3 times that of WT motor neurons which will amplify the synaptic potential for a given synaptic current by ~ 3.7 fold according to the model described by Lev-Tov et al.⁵⁴. Therefore, the ~ 5 fold reduction in the amplitude of primary afferent-evoked synaptic potentials in SMA motor neurons actually reflects a much greater reduction (~ 18 fold i.e. 5×3.7) in the amplitude of the synaptic currents, which is in agreement with our previous study¹³.

Functional assessment of the NMJ

To functionally assess neuromuscular junctions of the QL muscle at P4, we developed a technique by which motor neurons axons in the ventral root L2 supplying the QL muscle were stimulated, by drawing the ventral root into a suction electrode - having removed the spinal cord - and recorded the compound muscle action potential (CMAP) from the muscle, using a concentric bipolar electrode. L2 motor neuron axons were stimulated with a single stimulus at 0.1 Hz or at 20 Hz to emulate the physiological range of neonatal motor neurons' firing. The maximum CMAP amplitude (baseline-to-peak) was measured from 3–5 averages.

Somatodendritic labeling of motor neurons

Experimental protocols used in this study have been described before¹³. 101 mice of 0 to 11 days of age were used in tracing and immunohistochemistry experiments [24 WT, 21 SMA, 21 SMA+Pv^{Cre}, 17 SMA+ChAT^{Cre}, 12 SMA+(Pv+ChAT)^{Cre}, 6 Pv^{TeNT}]. The spinal cord was transferred to a dissection chamber and the L2 or L5 ventral root was placed inside a suction electrode and backfilled with a fluorescent dextran to label the motor neurons (Supplementary Table 2). Spinal cords from P0 – P5 animals were intact while P11 spinal cords were hemisected to improve oxygenation. The cord was perfused with cold (~10°C), oxygenated (95% O₂, 5% CO₂) aCSF (containing in mM: 128.35 NaCl, 4 KCl, 0.58 NaH₂PO₄·H₂O, 21 NaHCO₃, 30 D-Glucose, 0.1 CaCl₂·H₂O, and 2 MgSO₄·7H₂O). After 12 – 16 hours the cord was immersion-fixed in 4% PFA and washed in 0.01M phosphate buffer saline (PBS). Sections were subsequently processed for immunohistochemistry as described below and in Supplementary Table 2.

Retrograde labeling of muscle-identified motor neurons

Motor neurons supplying the IL and QL muscles were retrogradely labeled *in vivo* by intramuscular injection of cholera toxin B subunit (CTb) conjugated to Alexa 488. Newborn (P0) mice were anesthetized by isoflurane inhalation. A small incision in the left iliac (inguinal) area was made to access the IL/QL muscles, taking care not to puncture the peritoneum. The muscles were injected with ~1 µl of 1% CTb-Alexa 488 in PBS using a finely-pulled glass microelectrode. The CTb was delivered by pressure to an adapted micro-syringe. The incision was closed with sutures. The spinal cord was harvested at P4 following verification by fluorescence of accurate injection of CTb in the muscles and processed for immunohistochemistry.

Overexpression of BDNF in SMA mice

SMA mutant mice at P0 were anaesthetized by isoflurane (by inhalation) and injected intracerebro-ventricularly (ICV) with 10µl of 7.5×10¹³ GC/ml AAV2/9-CMV-GFP-2A-mBDNF virus (Vector BioLabs) at birth (P0), using a modified Hamilton syringe. Pups were allowed to recover from anesthesia for 30 min before returned to the cage. Mice were sacrificed at P5 for physiological or morphological experiments. For morphological experiments, the spinal cord and lumbar DRGs were immersion fixed in 4% PFA overnight. The L2 spinal segments and L2 DRGs were cut in 70µm thick sections using a Vibratome. GAD65 and GAD67 antibodies (kind gift from the Jessell lab) were used, together with the VGluT1 antibody, to visualize GABApre synapses on VGluT1+ synapses in SMA mice injected with AAV9-BDNF and SMA controls, as in³². GFP was amplified using chicken anti-GFP (Aves Labs) in 1:1000 concentration following overnight incubation. The anti-GFP was visualized with donkey anti-chicken Alexa-488 secondary antibody for 3 hours. The sections were scanned at the confocal microscope. Details and the efficacy of such method are included in our previous study³².

Immunohistochemistry

Some immunohistochemical protocols used in this study have been previously described^{13,32}. Details for new fixatives and immunohistochemical protocols used in this

study are included in Supplementary Table 2. All antibodies, except VGluT1, are commercially available. VGluT1 anti-guinea pig antibody was produced by Covance designed against the epitope (C)GATHSTVQPPRPPPP which lies within the n-terminus of mouse VGluT1. Spinal cords were embedded in warm 5% Agar and serial transverse sections were cut on a Vibratome (75 μ m thickness). Sections were blocked with 10% normal donkey serum in 0.01M PBS with 0.1% Triton X-100 (PBS-T; pH 7.4) and incubated overnight at room temperature in different combinations of antisera in PBS-T (Supplementary Table 2). For experiments involving anti-mouse antibodies, sections were pre-incubated for 1 hour in M.O.M blocker (Vector Laboratories) in PBS-T to block endogenous antigens. The following day, sections were washed in PBS-T and secondary antibody incubations were performed for 3 hours with the appropriate species-specific antiserum diluted in PBS-T. Sections were subsequently washed in PBS, mounted on glass slides using Vectashield (Vector Laboratories).

For the Kv2.1 immunoreactivity experiments, we used the K89/34 mouse IgG1 antibody (NeuroMab; mAb binds within aa 837–853; NeuroMab; cat #73-014 RRID:AB10672253). For the Kv2.2 immunoreactivity experiments, we used the N372B/1 mouse IgG1 antibody (NeuroMab; mAb binds within aa 764–907, cat#73-369, RRID:AB_2315869). Both antibodies have been verified to be specific by testing on Kv2.1 and Kv2.2 knockout mice⁵⁵ (see also: for Kv2.1: http://neuromab.ucdavis.edu/datasheet/K89_34.pdf; and for Kv2.2: http://neuromab.ucdavis.edu/datasheet/N372B_1.pdf). We also verified specificity of the Kv2.1 immunoreactivity on Kv2.1 knockout mouse spinal cord (kind gift by James Trimmer).

Neuromuscular junctions (NMJs) were analyzed in the QL muscle (Supplementary Table 2). Muscles from P4 mice from each genotype were fixed with 4% PFA for 20 mins and transferred to PBS. Single fibers were teased using fine forceps and washed for 30 mins in PBS supplemented with 0.1M glycine. Fibers were incubated with alpha-bungarotoxin-555 antibody for 20 mins and washed in PBS before permeabilization with ice-cold methanol at -20°C for 2 mins. Fibers were washed in PBS and incubated in a blocking solution containing 10% Donkey Serum in 0.3% PBS-T for an hour before treatment with anti-neurofilament and anti-synaptophysin at 4°C overnight. Samples were washed with PBS before incubation with the appropriate secondary antibodies for an hour (Supplementary Table 2). Fibers were washed and mounted in Vectashield.

Imaging and analysis

Sections were imaged using an SP5 Leica confocal microscope and analyzed using LASAF software (Leica). For all immunohistochemical analysis, at least three animals were used for each genotype. For SMN quantification, the number of motor and proprioceptive neurons with either present or absent nuclear Gems from L1 – L3 spinal segments were counted using a $\times 40$ objective from z-stacks (0.5 μ m steps) scans. At least 30 motor and proprioceptive neurons were included from each animal for each genotype. For motor neuron counts, we analyzed z-stacks images (at 3 μ m intervals) collected for each section that contained a fluorescent signal from L2 retrogradely labeled motor neurons as previously described for L1 motor neurons¹³. Sections were scanned using a $\times 20$ objective. Only motor

neurons (ChAT+) that contained the nucleus were counted in order to avoid double counting of adjoining sections.

Quantitative analysis of VGluT1 immunoreactive synaptic densities on motor neurons at P4 and P11 were performed on stacks of optical sections scanned using an $\times 40$ objective throughout the whole section thickness at $0.35 \mu\text{m}$ z-steps to include the whole cell body and dendrites of retrogradely labeled and ChAT+ motor neurons. To obtain density estimates, we measured all VGluT1+ contacts on dendritic segments at $50 \mu\text{m}$ sequential distances (0–50, 50–100, 100–150) from the cell body and divided this number by the total linear length of all dendritic segments in each compartment as described previously¹³. For VGluT1 motor neuron soma counts, only motor neurons with a whole cell body present within the z-stack were included.

To determine the extent of NMJ innervation, NMJ synapses were acquired using an $\times 20$ objective and z-stack images were scanned at $2 \mu\text{m}$ intervals. Images were analyzed off-line using LASAF software. NMJs were only considered innervated if the presynaptic nerve terminal completely co-localized with the postsynaptic endplate.

Analysis of Kv2.1 and Kv2.2 channels were performed from single optical plane images acquired with an $\times 63$ oil objective at 4096×4096 dpi resolution using an SP5 Leica confocal microscope. Only motor neuron somata (identified by ChAT immunoreactivity) in which the nucleus was present were included in the analysis. To calculate the coverage by Kv channel on motor neuron soma, a line was drawn along the soma perimeter to acquire the fluorescence intensity (expressed in arbitrary units), avoiding the area in which primary dendrites were present using LAS X software (Leica). A baseline fluorescence intensity measurement was achieved by drawing a straight line within the cytoplasm. The fluorescence intensity measurements were exported into Excel as x–y coordinates (x: distance in μm ; y: fluorescence intensity in arbitrary units). The fluorescence signal above 3 Standard Deviations (SD) of the baseline intensity measurement was considered expression of Kv immunoreactivity along the soma perimeter (Supplementary Fig. 14C), whereas the signal below was considered as background. The distance with fluorescence intensity above 3 standard deviations was calculated for each motor neuron and Kv channel coverage was expressed as a percentage of the total perimeter of the motor neuron soma.

Staining intensity measurements

Images of synaptic terminals were acquired on a Leica SP8 confocal microscope using a $40\times$ objective with $5\times$ digital zoom at a 2048×2048 optical resolution. Acquisition settings for excitation and fluorescence detection parameters were identical for each genotype, SMA controls and SMA+AAV9-BDNF. The GAD65 and GAD67 terminals were analyzed within a $10 \mu\text{m}$ confocal z-stack at 300 nm step intervals. Surface area and staining intensities were determined using Leica LAS AF imaging software. Relative synaptic protein levels were quantified by assessing the mean gray values, defined as the sum of the gray values of all the pixels in a region of interest (pixel sum), divided by the number of pixels in that region (pixel count), as we reported recently³². Regions of interest were defined as the outline of positively stained terminals. To quantify the relative levels of GABApre synaptic proteins

(GAD65 and GAD67), only varicosities directly juxtaposed to proprioceptive afferent terminals (VGluT1+) were considered.

Western blot analysis

The ventral horns from L1–L3 spinal cords WT and SMA mice (n=2) at P4 was removed under the microscope. Protein was homogenized in lysis buffer (150 mM NaCl, 1% Triton, 2 mM EDTA, 50 mM Tris, pH7.4). 20 µg protein extract was electrophoresed on a 12% SDS-PAGE gel and blotted for 40 mins to a PVDF membrane. The membranes were blocked for 1 hour with 5% skim milk and then probed with mouse anti-SMN (1:10,000, B&D), mouse anti-Tubulin (1:50 000, clone DM1A, Sigma) and mouse anti-Kv2.1 (1:5, NeuroMab) in blocking buffer overnight at 4°C. Subsequently, the membranes were washed 3 times with PBS and incubated with appropriate HRP-conjugated secondary antibodies (Jackson ImmunoResearch Laboratories) in PBS-T for 1 hour at room temperature. After 3 sequential 10 mins washes, enhanced chemiluminescence (GE Healthcare, Lifesciences) was used to for visualization.

Statistics

Results are expressed as means ± standard error of the mean (SEM). Statistical analysis was performed using GraphPad Prism 6. Comparison was performed by either Student's t-test or One-Way ANOVA (post-hoc comparison methods are indicated in the Results and figure legends when necessary). A statistical significance was considered P<0.05. Note that the D'Agostino & Pearson omnibus normality test was used to assess the normality for all data. If violated, non-parametric tests were used. No statistical methods were used to pre-determine sample sizes but our sample sizes are similar to those reported in previous publications^{13,20,41,53}. No randomization was used. Data collection and analysis were not performed blind to the conditions of the experiments.

The data that support the findings of this study are available from the corresponding author upon reasonable request.

Supplementary Material

Refer to Web version on PubMed Central for supplementary material.

Acknowledgments

We thank Martyn Goulding (Salk Institute) for generously providing the R26floxstop-TeNT mice. We also thank Susan Morton (Jessel lab) for her help with VGluT1 antibody production. We would like to thank Christoph Kellendonk (Columbia University) for his kind gift of the custom made Cre antibody. We are also grateful to James Trimmer (UC Davis) for his kind gift of Kv2.1 knockout mouse spinal cord tissue. We would like to thank T. Jessell, L. Pellizzoni, F.J. Alvarez, S. Przedborski, D. Logothetis, S. Schorge and F. Polleux for critical comments on the manuscript. G.Z.M. was supported by the NINDS, NIH (RO1-NS078375, R21-NS079981, R21-NS084185), the Department of Defense (GR.10235006), The SMA Foundation, Cure SMA, SMA-Europe and Target-ALS.

References

1. Jessell TM. Neuronal specification in the spinal cord: inductive signals and transcriptional codes. *Nat Rev Genet.* 2000; 1:20–29. [PubMed: 11262869]

2. Bleckert A, Wong RO. Identifying roles for neurotransmission in circuit assembly: insights gained from multiple model systems and experimental approaches. *Bioessays*. 2011; 33:61–72. [PubMed: 21110347]
3. Chen HH, Hippenmeyer S, Arber S, Frank E. Development of the monosynaptic stretch reflex circuit. *Curr Opin Neurobiol*. 2003; 13:96–102. [PubMed: 12593987]
4. Garcia-Campmany L, Stam FJ, Goulding M. From circuits to behaviour: motor networks in vertebrates. *Curr Opin Neurobiol*. 2010; 20:116–125. [PubMed: 20138753]
5. Glover JC. Development of specific connectivity between premotor neurons and motoneurons in the brain stem and spinal cord. *Physiol Rev*. 2000; 80:615–647. [PubMed: 10747203]
6. Rademakers R, Neumann M, Mackenzie IR. Advances in understanding the molecular basis of frontotemporal dementia. *Nat Rev Neurol*. 2012; 8:423–434. [PubMed: 22732773]
7. Palop JJ, Mucke L. Amyloid-beta-induced neuronal dysfunction in Alzheimer's disease: from synapses toward neural networks. *Nat Neurosci*. 2010; 13:812–818. [PubMed: 20581818]
8. Montes J, Gordon AM, Pandya S, De Vivo DC, Kaufmann P. Clinical outcome measures in spinal muscular atrophy. *J Child Neurol*. 2009; 24:968–978. [PubMed: 19509409]
9. Lefebvre S, et al. Identification and characterization of a spinal muscular atrophy-determining gene. *Cell*. 1995; 80:155–165. [PubMed: 7813012]
10. Tisdale S, Pellizzoni L. Disease mechanisms and therapeutic approaches in spinal muscular atrophy. *J Neurosci*. 2015; 35:8691–8700. [PubMed: 26063904]
11. Gavrilina TO, et al. Neuronal SMN expression corrects spinal muscular atrophy in severe SMA mice while muscle-specific SMN expression has no phenotypic effect. *Hum Mol Genet*. 2008; 17:1063–1075. [PubMed: 18178576]
12. Lotti F, et al. An SMN-dependent U12 splicing event essential for motor circuit function. *Cell*. 2012; 151:440–454. [PubMed: 23063131]
13. Mentis GZ, et al. Early functional impairment of sensory-motor connectivity in a mouse model of spinal muscular atrophy. *Neuron*. 2011; 69:453–467. [PubMed: 21315257]
14. Ling KK, Gibbs RM, Feng Z, Ko CP. Severe neuromuscular denervation of clinically relevant muscles in a mouse model of spinal muscular atrophy. *Hum Mol Genet*. 2012; 21:185–195. [PubMed: 21968514]
15. Zwambag DP, Ricketts TA, Brown SH. Sarcomere length organization as a design for cooperative function amongst all lumbar spine muscles. *J Biomech*. 2014; 47:3087–3093. [PubMed: 25042329]
16. Bácskai T, Rusznák Z, Paxinos G, Watson C. Musculotopic organization of the motor neurons supplying the mouse hindlimb muscles: a quantitative study using Fluoro-Gold retrograde tracing. *Brain Struct Funct*. 2014; 219:303–321. [PubMed: 23288256]
17. Alvarez FJ, Villalba RM, Zerda R, Schneider SP. Vesicular glutamate transporters in the spinal cord, with special reference to sensory primary afferent synapses. *J Comp Neurol*. 2004; 472:257–280. [PubMed: 15065123]
18. Rotterman TM, Nardelli P, Cope TC, Alvarez FJ. Normal distribution of VGLUT1 synapses on spinal motoneuron dendrites and their reorganization after nerve injury. *J Neurosci*. 2014; 34:3475–3492. [PubMed: 24599449]
19. Lutz CM, et al. Postsymptomatic restoration of SMN rescues the disease phenotype in a mouse model of severe spinal muscular atrophy. *J Clin Invest*. 2011; 121:3029–3041. [PubMed: 21785219]
20. Martinez TL, et al. Survival motor neuron protein in motor neurons determines synaptic integrity in spinal muscular atrophy. *J Neurosci*. 2012; 32:8703–8715. [PubMed: 22723710]
21. McGovern VL, et al. SMN expression is required in motor neurons to rescue electrophysiological deficits in the SMN 7 mouse model of SMA. *Hum Mol Genet*. 2015; 24:5524–5541. [PubMed: 26206889]
22. Mendelsohn AI, Simon CM, Abbott LF, Mentis GZ, Jessell TM. Activity regulates the incidence of heteronymous sensory-motor connections. *Neuron*. 2015; 87:111–123. [PubMed: 26094608]
23. Altman, J., Bayer, SA. *Development of the cerebellar system*. CRC Press; New York: 1997.

24. Hesse B, Fischer MS, Schilling N. Distribution pattern of muscle fiber types in the perivertebral musculature of two different sized species of mice. *Anat Rec (Hoboken)*. 2010; 293:446–463. [PubMed: 20169566]
25. Liu Q, Dreyfuss G. A novel nuclear structure containing the survival of motor neurons protein. *EMBO J*. 1996; 15:3555–3565. [PubMed: 8670859]
26. Li Y, Burke RE. Short-term synaptic depression in the neonatal mouse spinal cord: effects of calcium temperature. *J Neurophysiol*. 2001; 85:2047–2062. [PubMed: 11353021]
27. Umemiya M, Araki I, Kuno M. Electrophysiological properties of axotomized facial motoneurons that are destined to die in neonatal rats. *J Physiol (Lond)*. 1993; 462:661–678. [PubMed: 8392577]
28. Wainger BJ, et al. Intrinsic membrane hyperexcitability of amyotrophic lateral sclerosis patient-derived motor neurons. *Cell Rep*. 2014; 7:1–11. [PubMed: 24703839]
29. Humeau Y, Doussau F, Grant NJ, Poulain B. How botulinum and tetanus neurotoxins block neurotransmitter release. *Biochimie*. 2000; 82:427–446. [PubMed: 10865130]
30. Zhang Y, et al. V3 spinal neurons establish a robust and balanced locomotor rhythm during walking. *Neuron*. 2008; 60:84–96. [PubMed: 18940590]
31. Betley JN, et al. Stringent specificity in the construction of a GABAergic presynaptic inhibitory circuit. *Cell*. 2009; 139:161–174. [PubMed: 19804761]
32. Mende M, et al. Sensory-derived glutamate regulates presynaptic inhibitory terminals in mouse spinal cord. *Neuron*. 2016; 90:1189–1202. [PubMed: 27263971]
33. Gao BX, Ziskind-Conhaim L. Development of ionic currents underlying changes in action potential waveforms in rat spinal motoneurons. *J Neurophysiol*. 1998; 80:3047–3061. [PubMed: 9862905]
34. Herrington J, et al. Blockers of the delayed-rectifier potassium current in pancreatic beta-cells enhance glucose-dependent insulin secretion. *Diabetes*. 2006; 55:1034–1042. [PubMed: 16567526]
35. Liu PW, Bean BP. Kv2 channel regulation of action potential repolarization and firing patterns in superior cervical ganglion neurons and hippocampal CA1 pyramidal neurons. *J Neurosci*. 2014; 34:4991–5002. [PubMed: 24695716]
36. Lee JK, et al. Decursin attenuates kainic acid-induced seizures in mice. *Neuroreport*. 2014; 25:1243–1249. [PubMed: 25171200]
37. Kuo JJ, et al. Hyperexcitability of cultured spinal motoneurons from presymptomatic ALS mice. *J Neurophysiol*. 2004; 91:571–575. [PubMed: 14523070]
38. Powers RK, Binder MD. Input-output functions of mammalian motoneurons. *Rev Physiol Biochem Pharmacol*. 2001; 143:137–263. [PubMed: 11428264]
39. Redman S. Junctional mechanisms at group Ia synapses. *Prog Neurobiol*. 1979; 12:33–83. [PubMed: 93760]
40. Devlin AC, et al. Human iPSC-derived motoneurons harbouring TARDBP or C9ORF72 ALS mutations are dysfunctional despite maintaining viability. *Nat Commun*. 2015; 6:5999. [PubMed: 25580746]
41. Gogliotti RG, et al. Motor neuron rescue in spinal muscular atrophy mice demonstrates that sensory-motor defects are a consequence, not a cause, of motor neuron dysfunction. *J Neurosci*. 2012; 32:3818–3829. [PubMed: 22423102]
42. Kernell D. The limits of firing frequency in cat lumbosacral motoneurons possessing different time course of afterhyperpolarization. *Acta Physiol Scand*. 1965; 65:87–100.
43. Scannevin RH, Murakoshi H, Rhodes KJ, Trimmer JS. Identification of a cytoplasmic domain important in the polarized expression and clustering of the Kv2.1 K⁺ channel. *J Cell Biol*. 1996; 135:1619–1632. [PubMed: 8978827]
44. Muennich EA, Fyffe RE. Focal aggregation of voltage-gated, Kv2.1 subunit-containing, potassium channels at synaptic sites in rat spinal motoneurons. *J Physiol (Lond)*. 2004; 554:673–685. [PubMed: 14608003]
45. Romer SH, et al. Redistribution of Kv2.1 ion channels on spinal motoneurons following peripheral nerve injury. *Brain Res*. 2014; 1547:1–15. [PubMed: 24355600]

46. Misonou H, et al. Regulation of ion channel localization and phosphorylation by neuronal activity. *Nat Neurosci.* 2004; 7:711–718. [PubMed: 15195093]
47. De Luca CJ, LeFever RS, McCue MP, Xenakis AP. Behaviour of human motor units in different muscles during linearly varying contractions. *J Physiol (Lond).* 1982; 329:113–128. [PubMed: 7143246]
48. Thomas CK. Human motor units studied by spike-triggered averaging and intraneural motor axon stimulation. *Adv Exp Med Biol.* 1995; 384:147–160. [PubMed: 8585447]
49. Ritter LK, Tresch MC, Heckman CJ, Manuel M, Tysseling VM. Characterization of motor units in behaving adult mice shows a wide primary range. *J Neurophysiol.* 2014; 112:543–551. [PubMed: 24805075]
50. De Luca CJ. Control properties of motor units. *J Exp Biol.* 1985; 115:125–136. [PubMed: 4031760]
51. Hippenmeyer S, et al. A developmental switch in the response of DRG neurons to ETS transcription factor signaling. *PLoS Biol.* 2005; 3:e159. [PubMed: 15836427]
52. Isokawa M. Membrane time constant as a tool to assess cell degeneration. *Brain Res Brain Res Protoc.* 1997; 1:114–116. [PubMed: 9385072]
53. Shneider NA, Mentis GZ, Schustak J, O'Donovan MJ. Functionally reduced sensorimotor connections form with normal specificity despite abnormal muscle spindle development: the role of spindle-derived neurotrophin 3. *J Neurosci.* 2009; 29:4719–4735. [PubMed: 19369542]
54. Lev-Tov A, Miller JP, Burke RE, Rall W. Factors that control amplitude of EPSPs in dendritic neurons. *J Neurophysiol.* 1983; 50:399–412. [PubMed: 6310060]
55. Bishop HI, et al. Distinct cell- and layer-specific expression patterns and independent regulation of Kv2 channel subtypes in cortical pyramidal neurons. *J Neurosci.* 2015; 35:14922–14942. [PubMed: 26538660]
56. Kellendonk C, et al. Inducible site-specific recombination in the brain. *J Mol Biol.* 1999; 285:175–182. [PubMed: 9878397]

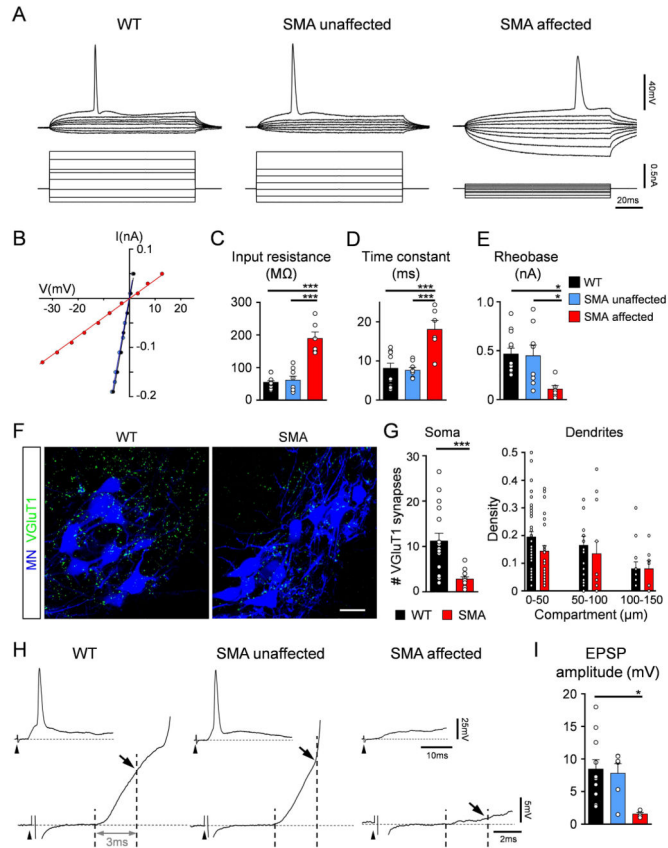


Figure 1. Early dysfunction in a subset of vulnerable SMA motor neurons

(A) Membrane responses (top) following current injection (bottom) in a WT, an SMA-unaffected and an SMA-affected motor neuron.

(B) Current/voltage relationship for a WT (black), an SMA-unaffected (blue) and an SMA-affected (red) motor neuron.

(C) The average input resistance for WT (n=12), SMA-unaffected (n=8) and SMA-affected (n=6) motor neurons at P2. *** P<0.001, one-way ANOVA, Tukey's *post hoc* analysis (WT v SMA-affected; SMA-unaffected v SMA-affected).

(D) The average time constant for WT (n=12), SMA-unaffected (n=8) and SMA-affected (n=6) motor neurons. *** P<0.001, one-way ANOVA, Tukey's *post hoc* analysis (WT v SMA-affected; SMA-unaffected v SMA-affected).

(E) The average rheobase for WT (n=12), SMA-unaffected (n=8) and SMA affected (n=6) motor neurons. * P<0.05, one-way ANOVA, Tukey's *post hoc* analysis (WT v SMA-affected; SMA-unaffected v SMA-affected).

(F) Z-stack projection of confocal images from retrogradely labeled L2 motor neurons (blue) and VGlut1 synaptic boutons (green) in a WT and a SMA mouse at P2. The total distance in the z axis for the WT and the SMA was 7 μ m (20 optical planes at 0.35 μ m intervals).

(G) The average number of VGlut1 boutons on the entire soma (left) and synaptic dendritic density (right) in 50 μ m dendritic compartments from the soma, for WT (n=17) and SMA (n=13) motor neurons. *** P<0.001, unpaired t-test (soma); N.S. for dendrites, t-test for 0–50 μ m and Mann-Whitney for 50–100 and 100–150 μ m dendritic compartments.

(H) Intracellular responses after supramaximal stimulation of the L2 dorsal root in a WT, SMA-unaffected and SMA-affected motor neuron at P2 shown in insets. The monosynaptic part of the EPSP is shown on an expanded timescale for each neuron (vertical dotted lines). Arrows indicate the maximum EPSP amplitude and arrowheads the stimulus artifact.

(I) Average EPSP peak amplitude for WT (n=11), SMA-unaffected (n=6) and SMA-affected (n=4) motor neurons. * P<0.05, one-way ANOVA, Tukey's *post hoc* analysis (WT v SMA-affected).

All data are represented as mean \pm s.e.m. * P<0.05, ** P<0.01, *** P<0.001, N.S., not significant (P>0.05). For details, see online methods checklist.

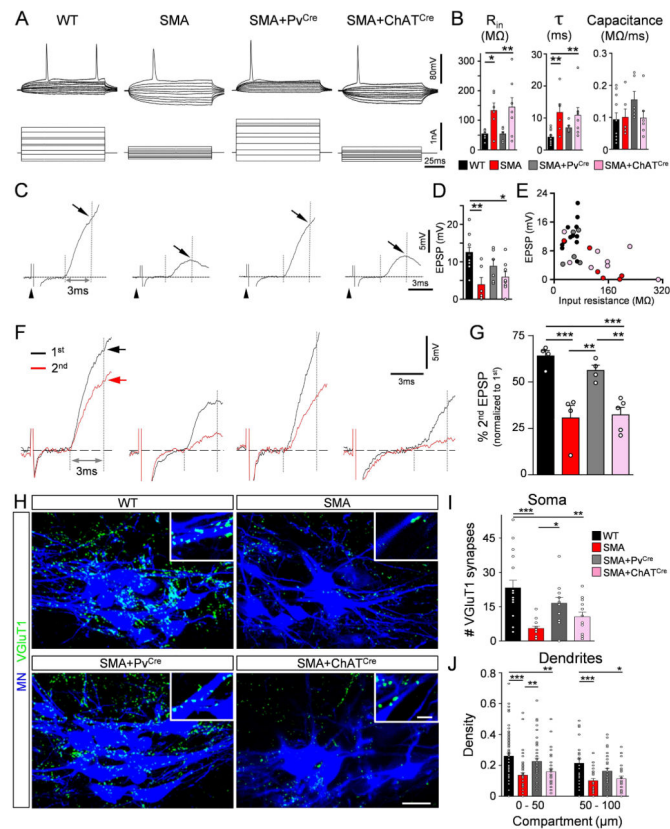


Figure 2. Selective upregulation of SMN in proprioceptive neurons only, normalizes motor neuron membrane hyperexcitability and VGlut1 synapses

(A) Membrane responses (top) following current injection (bottom) in WT, SMA, SMA+Pv^{Cre} and SMA+ChAT^{Cre} L2 motor neurons at P4.

(B) The average input resistance (R_{in}), membrane time constant (τ) and capacitance in WT (n=11), SMA (n=6), SMA+Pv^{Cre} (n=6) and SMA+ChAT^{Cre} (n=8) L2 motor neurons. * $P < 0.05$, ** $P < 0.01$, one-way ANOVA, Tukey's *post hoc* analysis (WT v SMA and WT v SMA+ChAT^{Cre}).

(C) Intracellular responses of monosynaptic EPSPs following supramaximal stimulation of the L2 dorsal root in homonymous motor neurons for the same groups shown in (A). Arrows indicate the peak EPSP amplitude measured at 3 ms after the onset of response and arrowheads the stimulus artifact.

(D) The average peak EPSP amplitude in motor neurons for the experimental groups shown in (C). * $P < 0.05$, ** $P < 0.01$, one-way ANOVA, Tukey's *post hoc* analysis (WT v SMA and WT v SMA+ChAT^{Cre}).

(E) Relationship between peak EPSP amplitude and input resistance of L2 motor neurons for the experimental groups shown in (A).

(F) 1st (black) and 2nd (red) EPSP responses elicited in motor neurons after 1 Hz dorsal root stimulation in the experimental groups shown in (A). Arrows indicate the peak EPSP amplitude measured at 3 ms after the onset of response.

(G) Average percentage of 2nd EPSP response, normalized to 1st response by motor neurons in the experimental groups shown in (F). ** $P < 0.01$, *** $P < 0.001$, one-way ANOVA, Tukey's *post hoc* analysis.

(H) Z-stack projection of confocal images from retrogradely labeled L2 motor neurons (blue) and VGluT1 synaptic boutons (green) in a WT, SMA, SMA+Pv^{Cre} and SMA+ChAT^{Cre} mouse at P4. Insets show VGluT1 synaptic appositions on dendrites at higher magnification. The total distance in the z axis for all images was 7 μm (20 optical planes at 0.35 μm intervals) and for the insets 1.5 μm .

(I) The average number of VGluT1 boutons on somata of L2 WT (n=17), SMA (n=14), SMA+Pv^{Cre} (n=13) and SMA+ChAT^{Cre} (n=15) motor neurons. * P<0.05, ** P<0.01, *** P<0.001, one-way ANOVA, Tukey's *post hoc* analysis (WT v SMA; WT v SMA+ChAT^{Cre} and SMA v SMA+Pv^{Cre}).

(J) VGluT1 synaptic density on 50 μm dendritic compartments from the soma, for the same groups shown in (G). * P<0.05, ** P<0.01, *** P<0.001, one-way ANOVA, Tukey's *post hoc* analysis (WT v SMA; WT v SMA+ChAT^{Cre} and SMA v SMA+Pv^{Cre}).

All data are represented as mean \pm s.e.m. For details, see online methods checklist.

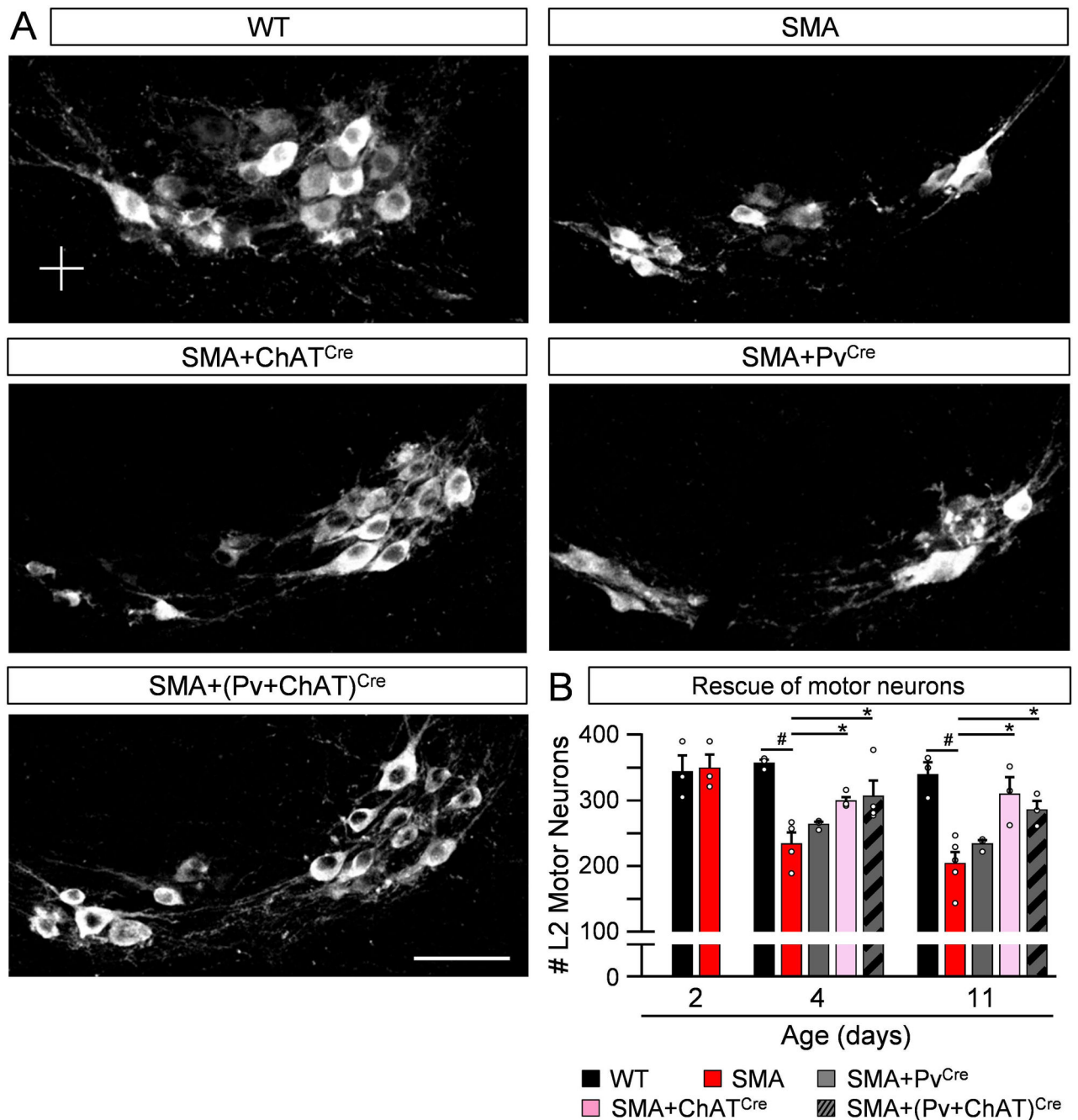


Figure 3. Motor neuron loss due to SMN deficiency is mediated by cell autonomous mechanisms
 (A) Confocal images of WT (n=3), SMA (n=4), SMA+Pv^{Cre} (n=3), SMA+ChAT^{Cre} (n=4) and SMA+(Pv+ChAT)^{Cre} (n=4) L2 motor neurons visualized by ChAT immunoreactivity at P4.

(B) Time course (P2–P11) of the total number of L2 motor neurons for the experimental groups shown in (A). All data are represented as mean ± s.e.m. # P<0.05, one-way ANOVA (WT v SMA); * P<0.05, one-way ANOVA, Tukey's *post hoc* analysis [SMA v SMA +ChAT^{Cre} and SMA v SMA+(Pv+ChAT)^{Cre}]. For details, see online methods checklist.

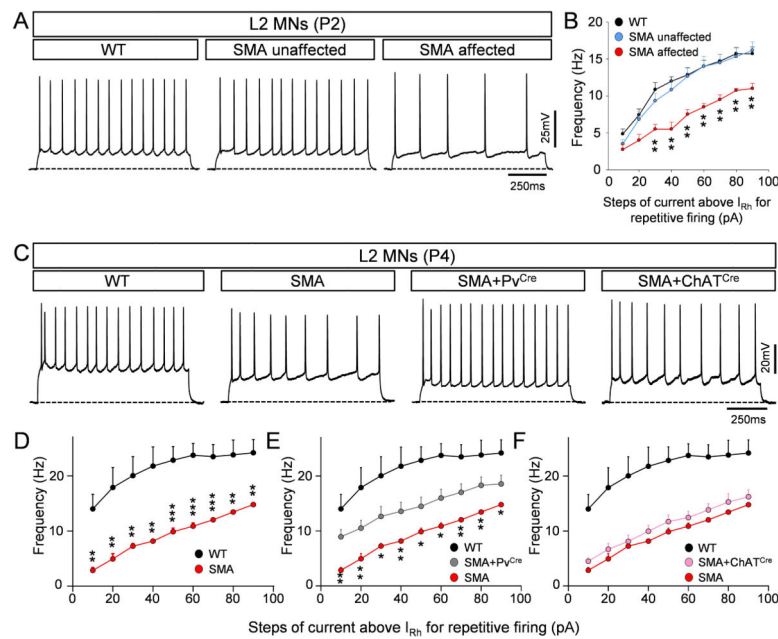


Figure 4. Significant improvement of reduced firing frequency in SMA motor neurons following selective upregulation of SMN in proprioceptive neurons only

(A) Intracellular responses of repetitive firing following 50 pA current injection above the minimum current required for continuous firing for a WT (n=7), SMA unaffected (n=6) and SMA affected (n=4) motor neuron at P2.

(B) Frequency-to-current relationship for the three groups shown in (A). * $P < 0.05$, ** $P < 0.01$, *** $P < 0.001$, one-way ANOVA, Tukey's *post hoc* analysis (WT v SMA-affected for individual steps of current). For details, see online methods checklist.

(C) Intracellular responses of repetitive firing following 50 pA current injection above the minimum current required for continuous spiking, in a WT, SMA, SMA+Pv^{Cre} and SMA+ChAT^{Cre} motor neuron at P4.

(D) Frequency-to-current relationship for WT and SMA motor neurons at P4. ** $P < 0.01$, *** $P < 0.001$, unpaired t-test for the individual steps of current (WT v SMA).

(E) Frequency-to-current relationship for WT, SMA and SMA+Pv^{Cre} motor neurons at P4. * $P < 0.05$, ** $P < 0.01$, unpaired t-test for the individual steps of current (SMA v SMA+Pv^{Cre}).

(F) Frequency-to-current relationship for WT, SMA and SMA+ChAT^{Cre} motor neurons at P4. NS, $P > 0.05$ (SMA v SMA+ChAT^{Cre}).

All data are represented as mean \pm s.e.m. For details, see online methods checklist.

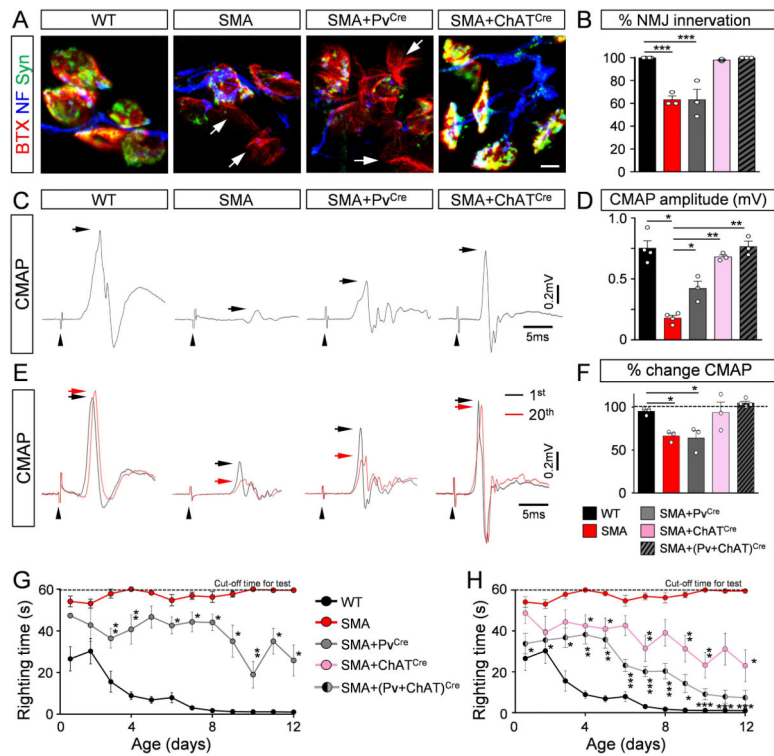


Figure 5. Improvement of NMJ function, innervation and behavioral benefits following selective restoration of SMN in proprioceptive and motor neurons

(A) Confocal images of NMJs from the QL muscle labeled by the presynaptic markers synaptophysin (green), neurofilament (blue) and the postsynaptic marker bungarotoxin (red) in WT, SMA, SMA+Pv^{Cre} and SMA+ChAT^{Cre} mice at P4. Arrows indicate denervated NMJs.

(B) Percentage extent of innervation of the QL muscle in WT (n=4), SMA (n=4), SMA+Pv^{Cre} (n=3), SMA+ChAT^{Cre} (n=3) and SMA+(Pv+ChAT)^{Cre} (n=3). *** P<0.001, one-way ANOVA, Tukey's *post hoc* analysis (WT v SMA and WT v SMA+Pv^{Cre}).

(C) Compound muscle action potentials (CMAP) recorded from the QL muscle following stimulation of the L2 ventral root in WT, SMA, SMA+Pv^{Cre} and SMA+ChAT^{Cre} mice at P4. Arrows indicate the peak CMAP amplitude and arrowheads the stimulus artifact.

(D) Average of peak CMAP amplitude for the experimental groups shown in (C). * P<0.05, ** P<0.01, one-way ANOVA, Tukey's *post hoc* analysis [WT v SMA, SMA v SMA+Pv^{Cre}, SMA v SMA+ChAT^{Cre} and SMA v SMA+(Pv+ChAT)^{Cre}].

(E) Compound muscle action potentials (CMAP) recorded from the QL muscle following 20 Hz stimulation of the L2 ventral root in WT, SMA, SMA+Pv^{Cre} and SMA+ChAT^{Cre} mice at P4. The 1st (black) and 20th (red) CMAP are shown superimposed. Horizontal arrows indicate the peak CMAP amplitude and arrowheads the stimulus artifact.

(F) Percentage change of CMAP amplitude expressed as a ratio of the 20th/1st response in WT, SMA, SMA+Pv^{Cre}, SMA+ChAT^{Cre} and SMA+(Pv+ChAT)^{Cre} mice at P4. * P<0.05, one-way ANOVA, Tukey's *post hoc* analysis (WT v SMA and WT v SMA+Pv^{Cre}).

(G) Righting times for WT (black), SMA (red) and SMA mice in which SMN was restored in proprioceptive neurons only (SMA+Pv^{Cre}; grey). * P<0.05, ** P<0.01, t-test SMA+Pv^{Cre} v SMA for the individual ages.

(H) Righting times for WT (black), SMA (red), SMA mice in which SMN was restored in motor neurons only (SMA+ChAT^{Cre}; pink), and SMA mice in which SMN was restored in both proprioceptive and motor neurons [SMA+(Pv+ChAT)^{Cre}; black/grey]. * P<0.05, ** P<0.01, *** P<0.001, unpaired t-test, [SMA v SMA+Pv^{Cre} and SMA v SMA+(Pv+ChAT)^{Cre}]. All data are represented as mean ± s.e.m. For details, see online methods checklist.

Author Manuscript

Author Manuscript

Author Manuscript

Author Manuscript

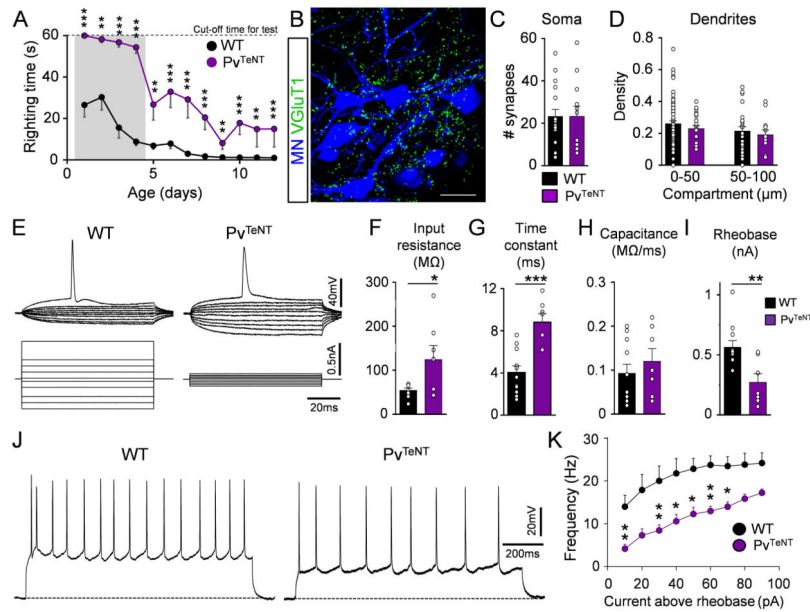


Figure 6. Neurotransmission block in proprioceptive neurons by tetanus toxin renders WT motor neurons dysfunctional

(A) Righting time for WT (black, n=14) and Pv^{TeNT} (violet, n=8) mice. ** $P < 0.01$, *** $P < 0.001$, unpaired t-test, (WT v Pv^{TeNT}) for the individual ages. Shaded area indicates the inability of righting in Pv^{TeNT} mice during the first four postnatal days.

(B) Z-stack projection of confocal images from retrogradely labeled L2 motor neurons (blue) and VGLuT1 synaptic boutons (green) in a Pv^{TeNT} mouse at P4. The total distance in the z-axis was 7 μm (20 optical planes at 0.35 μm intervals).

(C) The average number of VGLuT1 boutons on the entire soma of L2 WT and Pv^{TeNT} motor neurons.

(D) VGLuT1 synaptic density on 50 μm dendritic compartments from the soma, for WT and Pv^{TeNT} mice.

(E) Membrane responses (top) following current injection (bottom) in a WT and a Pv^{TeNT} L2 motor neurons at P4.

(F) The average input resistance for WT (n=11) and Pv^{TeNT} (n=7) motor neurons at P4. * $P = 0.0163$, unpaired t-test.

(G) The average membrane time constant for WT and Pv^{TeNT} motor neurons at P4. * $P = 0.0003$, unpaired t-test.

(H) The average capacitance for WT and Pv^{TeNT} motor neurons at P4.

(I) The average rheobase current for WT and Pv^{TeNT} motor neurons at P4. ** $P = 0.0056$, unpaired t-test.

(J) Intracellular responses of repetitive firing following 50 pA current injection above the minimum current required for continuous spiking, for a WT and a Pv^{TeNT} motor neuron at P4.

(K) Frequency-to-current relationships for WT and Pv^{TeNT} motor neurons at P4. * $P < 0.05$, ** $P < 0.01$, unpaired t-test at individual steps of current WT v Pv^{TeNT} .

All data are represented as mean \pm s.e.m. For details, see online methods checklist.

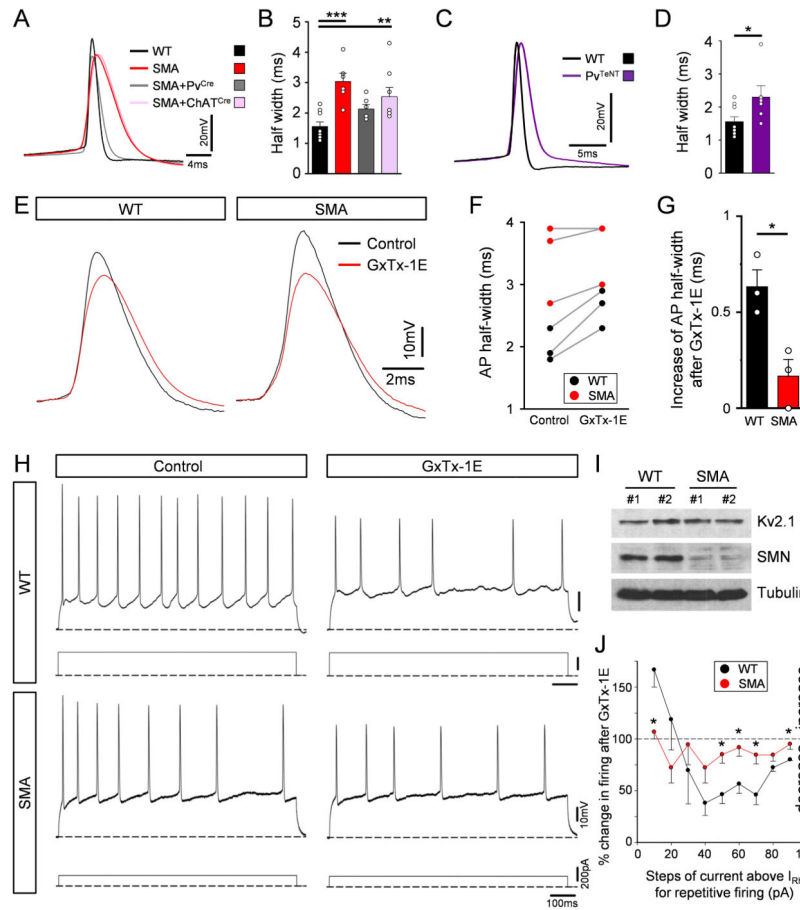


Figure 7. Prolonged action potentials through the delayed rectifier channels are associated with reduction in firing frequency in SMA and Pv^{TeNT} motor neurons

(A) Action potentials during steady-state firing following current injection in WT (black, n=8), SMA (red, n=6), SMA+Pv^{Cre} (grey, n=6) and SMA+ChAT^{Cre} (pink, n=8) L2 motor neurons at P4.

(B) The average duration of action potential half-width for the groups shown in (A). ** P<0.01, *** P<0.001, one-way ANOVA, Tukey's *post hoc* analysis (WT v SMA and WT v SMA+ChAT^{Cre}).

(C) Action potentials during steady-state firing following current injection in a WT (black, n=8) and a Pv^{TeNT} (violet, n=6) L2 motor neuron at P4.

(D) The average duration of half-width from action potentials for WT and Pv^{TeNT} motor neurons. * P=0.042, unpaired t-test.

(E) Superimposed action potentials before (black) and after (red) GxTx-1E (100 nM) exposure in a WT and an SMA motor neuron.

(F) Change of the action potential half-width before and after GxTx-1E exposure in WT (black) and SMA (red) motor neurons.

(G) Average increase in the action potential half-width following GxTx-1E exposure in WT (black) and SMA (red) motor neurons. * P=0.034, paired t-test.

(H) Intracellular responses following current injection in control solution and after GxTx-1E exposure in a WT and an SMA motor neuron.

(I) Western blot analysis for Kv2.1 (top), SMN (middle) and tubulin (bottom) protein expression from two WT and two SMA ventral spinal cords at P4. Blots have been cropped.

(J) Percentage change in firing frequency following GxTx-1E exposure at 10 pA steps of current injection for WT and SMA motor neurons. The relative increase or decrease in firing frequency is indicated on the right. * $P < 0.05$, unpaired t-test for the individual steps of current. All data are represented as mean \pm s.e.m. For details, see online methods checklist.

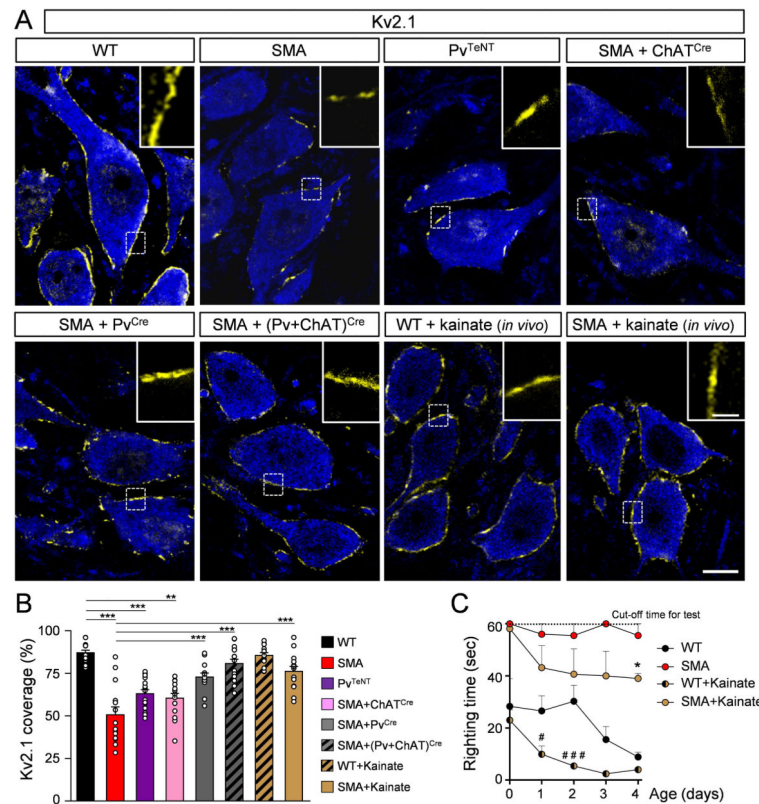


Figure 8. Loss of SMN from proprioceptors reduces the surface expression of Kv2.1 in motor neurons

(A) Single optical plane confocal images of L2 motor neurons (ChAT in blue) expressing Kv2.1 channels (yellow) for WT (n=14), SMA (n=14), Pv^{TeNT} (n=15), SMA+ChAT^{Cre} (n=14), SMA+Pv^{Cre} (n=13), SMA+(Pv+ChAT)^{Cre} (n=16) and WT (n=13) as well as SMA mice (n=14) treated *in vivo* with kainate, at P4. Insets show Kv2.1 immunoreactivity at higher magnification of the boxed dotted area.

(B) Percentage somatic coverage of Kv2.1 expression in motor neurons for the same experimental groups shown in (A). ** P<0.01, *** P<0.001, one-way ANOVA, Tukey's *post hoc* analysis [WT v SMA, WT v Pv^{TeNT}, WT v SMA+ChAT^{Cre}, SMA v SMA+Pv^{Cre}, SMA v SMA+(Pv+ChAT)^{Cre} and SMA v SMA+Kainate]. All data are represented as mean ± s.e.m. For details, see online methods checklist.

(C) Righting times following daily *in vivo* kainate treatment (1.5 mg/kg) for WT and SMA mice. * P<0.05, unpaired t-test, SMA untreated v SMA kainate treated mice. # P<0.05, and ### P<0.001, unpaired t-test, WT untreated v WT kainate treated mice.